

See discussions, stats, and author profiles for this publication at: <https://www.researchgate.net/publication/392021123>

Wind Tunnel Investigation of a Rotor Under the Influence of Unsteady Ship Airwakes with Azimuth-Correlated Measurements

Conference Paper · May 2025

DOI: 10.4050/F-0081-2025-47

CITATIONS

0

READS

225

2 authors:



Wei-Han Chen
Georgia Institute of Technology

7 PUBLICATIONS 28 CITATIONS

[SEE PROFILE](#)



Juergen Rauleder
Georgia Institute of Technology

102 PUBLICATIONS 610 CITATIONS

[SEE PROFILE](#)

Wind Tunnel Investigation of a Rotor Under the Influence of Unsteady Ship Airwakes with Azimuth-Correlated Measurements

Wei-Han Chen
Graduate Research Assistant

Juergen Rauleder
Assistant Professor

Georgia Institute of Technology
Atlanta, Georgia, USA

ABSTRACT

The performance and unsteady loads of a rotor operating in shipboard environments are highly sensitive to the influence of unsteady ship airwakes. In extreme cases, this interaction can significantly degrade rotorcraft handling qualities and constrain the safe launch and recovery flight envelope. This study presents wind tunnel measurements of azimuth-correlated rotor hub loads for a 1:100 scale single main rotor, modeled after the NATO Generic Rotorcraft, hovering above and around the landing deck of the NATO Generic Destroyer. These measurements were complemented with Particle Image Velocimetry (PIV) measurements. Unlike time-averaged data, azimuth-resolved measurements reveal detailed insights into the interactional aerodynamics between the rotor and ship airwake at specific rotor azimuth angles. By comparing phase-averaged rotor load responses to a trimmed reference condition measured up-and-away from the ship airwake, this study discovered both beneficial and detrimental load variations across different azimuth angles. These variations were strongly influenced by the hovering location of the rotor relative to the ship deck. While longitudinal shifts along the deck centerline resulted in gradual changes, lateral offsets induced significant changes in azimuthal thrust characteristics. Additionally, the wind-over-deck (WOD) angle had a considerable effect, with quartering wind conditions causing significant detrimental impacts on the upstream blades at certain azimuth angles, locally leading to a substantial loss of thrust. These findings were further supported by horizontal and vertical plane PIV measurements. Both the extracted downwash velocity data and local thrust estimates based on momentum conservation showed notable azimuthal and radial variations in downwash velocities and thrust production across the rotor disk, closely matching direct thrust measurements across different hovering conditions.

NOMENCLATURE

A	Rotor disk area (m^2)	T	Thrust (N)
A_f	Accumulated frontal area of test article (m^2)	\tilde{T}_{rms}	Normalized unsteady thrust, $\frac{\tilde{T}_{rms}}{T}$
A_t	Test section cross-sectional area (m^2)	U_∞	Freestream velocity (m/s)
C_T	Thrust coefficient, $\frac{T}{\rho(\pi R^2)(\Omega R)^2}$	V	Velocity magnitude (m/s)
C_{M_x}	Rolling moment coefficient, $\frac{M_x}{\rho(\pi R^2)(\Omega R)^2 R}$	\tilde{V}	Normalized velocity magnitude, $\frac{V}{U_\infty}$
C_{M_y}	Pitching moment coefficient, $\frac{M_y}{\rho(\pi R^2)(\Omega R)^2 R}$	c	Blade chord (m)
F_x, F_y, F_z	Rotor longitudinal, lateral, and axial force (N)	h	Height above landing deck (m)
I_T	Thrust index, $\tilde{w}_{disk} \cdot (\tilde{w}_{outflow} - \tilde{w}_{inflow})$	\dot{m}_z	Mass flow rate perpendicular across the rotor disk (kg/s)
M_x, M_y, M_z	Rotor rolling, pitching, and yawing moment (N·cm)	h_{hod}	Height at hover-over-deck (m)
M_{tip}	Rotor blade tip Mach number	p	Surface pressure (Pa)
N_b	Number of rotor blades	p_o	Reference pressure (Pa)
R	Rotor radius (m)	q_u, q_c	Uncorrected and corrected dynamic pressure (Pa)
Re_s	Ship beam Reynolds number, $\frac{U_\infty w_s}{v}$	w	Downwash velocity (m/s)
Re_{tip}	Rotor blade tip Reynolds number, $\frac{U_{tip} c}{v}$	w_{disk}	Downwash velocity at rotor disk (m/s)
		w_{inflow}	Inflow velocity above rotor disk (m/s)
		$w_{outflow}$	Outflow velocity below rotor disk (m/s)
		\bar{w}	Mean downwash velocity (m/s)
		\tilde{w}	Normalized mean downwash velocity, $\frac{\bar{w}}{U_\infty}$
		\tilde{w}_{disk}	Normalized downwash velocity at rotor disk, $\frac{w_{disk}}{U_\infty}$

Presented at the Vertical Flight Society's 81st Annual Forum & Technology Display, Virginia Beach, VA, USA, May 20–22, 2025. Copyright © 2025 by the authors except where noted. Published by the Vertical Flight Society with permission. All rights reserved.

\tilde{w}_{inflow}	Normalized inflow velocity above rotor disk, $\frac{\tilde{w}_{inflow}}{U_\infty}$
$\tilde{w}_{outflow}$	Normalized outflow velocity below rotor disk, $\frac{\tilde{w}_{outflow}}{U_\infty}$
w_s, l_s	Width and length of ship (m)
x, y, z	Longitudinal, lateral, and vertical positions (m)
θ	Blade twist angle (deg)
μ	Advance ratio, $\frac{U_\infty}{\Omega R}$
ρ	Air density (kg/m^3)
Ω	Rotor angular velocity (rad/s)
σ	Rotor solidity, $\frac{N_b c}{\pi R}$
ψ	Rotor azimuth angle (deg)
Ψ	Wind-over-deck angle (deg)
ν	Kinematic viscosity (m^2/s)

INTRODUCTION

During shipboard operations of rotorcraft, the highly unsteady interactions between the ship airwake and the rotor poses a significant challenge to helicopter pilots. Accompanied by the large ship motions at higher sea states, the unsteady airwake shed from the ship superstructure can greatly influence the forces experienced by the vehicle and rapidly alter the rotor inflow, causing significant increase in pilot workload. Throughout the past decades, this ship–rotor dynamic interface (DI) problem has raised great research interest in order to gain further understanding of the interactional aerodynamics and aid future pilot training by validating computational simulations through experimental studies.

In order to understand the fundamental characteristics of the ship airwake, several experimental studies of the simplified frigate shape (SFS), a simplified geometry that resembles a naval frigate, have been studied extensively. Sydney et al. (Ref. 1) assessed the highly turbulent and three-dimensional airwake through detailed particle image velocimetry (PIV) measurements along the entire length of the ship model and laterally across the landing deck region. Seth et al. (Ref. 2) studied the effect of a simulated atmospheric boundary layer in subscale experiments. Zhu et al. (Ref. 3) investigated the unique bistable behavior of the SFS airwake through proper orthogonal decomposition (POD) and conditional averaging of PIV measurements. Mazzilli et al. (Ref. 4) used reduced order modeling to compare the airwake between the SFS and the NATO Generic Destroyer (GD), which is a shared geometry for collaborative research introduced by the Canadian National Research Council (Ref. 5). Palm et al. (Ref. 6) further explored the airwake characteristics of the NATO-GD under different freestream conditions with oil flow visualization and comprehensive PIV measurements of the landing deck.

In addition to studies of the standalone ship airwake, researchers have extensively approached the DI problem with sub-scale experiments involving a rotor system to explore the unsteady aerodynamic phenomena and provide valuable validation data for modeling and simulations. Early efforts

by Zan (Ref. 7) involved wind tunnel experiments with a 1:50-scale model of the Canadian Patrol Frigate (CPF), and demonstrated that interactions between the rotor and ship airwake could significantly degrade time-averaged rotor thrust performance. The influence of the ship varied with the rotor's position above the landing deck and depended strongly on wind direction and speed. Additionally, unsteady loads acting on the rotor model were quantified by Lee (Ref. 8), revealing correlations between these loads and pilot workload from flight test data. Furthermore, due to an incident in which an on-deck V-22 experienced an uncommanded roll while a CH-46 was being recovered upwind, Silva et al. (Ref. 9) carried out experimental investigations involving multiple rotorcraft models to study the aerodynamic interactions between rotorcraft operating around a Landing Helicopter Assault (LHA) class ship. Loads and PIV measurements from this effort showed strong dependencies on the on-deck tiltrotor rolling moment response to the relative position of the upwind aircraft and wind-over-deck (WOD) conditions.

Approaching with a different setup, Wang et al. (Ref. 10) conducted experiments in a water tunnel, leveraging several advantages such the relative ease of generating higher Reynolds numbers that are more relevant to full-scale conditions. A dynamic force balance was custom-designed for a helicopter model to measure the unsteadiness of the ship wake. Utilizing the above-mentioned experimental setup, Kääriä et al. (Ref. 11) explored how different designs of the ship superstructure changed the performance of a rotor operating behind the ship. Nacakli et al. (Ref. 12) studied the ship–rotor coupled flow field using a backward-facing-step as a representative ship, similar to the SFS geometry. A PIV survey was conducted with thrust measurements of a rotor hovering at various positions above the landing deck along the symmetric plane of the ship in headwind. It was observed that the reingestion of the recirculated flow while hovering close to the hangar wall combined with the ground effect greatly influenced the rotor thrust performance.

Taymourtash et al. (Ref. 13) assessed the loads on a 1:13-scale Bo105 helicopter model in various positions along different trajectories towards the landing deck. Significant changes were seen in the helicopter moments along the path that were highly dependent on the wind direction as well. In a recent investigation by Silva et al. (Ref. 14), loads, PIV, and surface pressure measurements were carried out with V-22 and H-1 rotorcraft models hovering behind a 1:48-scale San Antonio class landing platform dock (LPD) in different configurations. The obtained results showed the thrust deficit while operating behind the ship superstructure and the changes in differential thrust controls required to compensate for the induced rolling moments on the V-22 model.

In addition to experimental efforts, researchers have employed various computational fluid dynamics (CFD) solvers to model the SFS and NATO-GD airwake and evaluate its impact on helicopter handling qualities (Refs. 15–18). By incorporating additional features on the superstructure and adopting a more realistic geometry, Fernandez et al. (Ref. 19) have shown that the NATO-GD produces distinct airwakes compared to the

SFS that interacting differently with helicopters. Ashok and Rauleder (Ref. 20) recently developed a two-way coupled mid-fidelity GPU-accelerated Lattice-Boltzmann real-time simulation model, which demonstrated good agreement with experimental data for a rotor operating behind the NATO-GD.

Although extensive experimental and computational efforts have been conducted, there are still areas that lack a fundamental understanding of the DI problem, specifically in how and where the ship airwake affects the rotor azimuthally. Thus, building upon a previous research effort (Ref. 21), this study conducted sub-scale wind tunnel experiments that measured rotor azimuth-correlated hub loads and stereoscopic PIV flow fields of a single main rotor hovering under different test configurations, including varying hovering locations and WOD angles. By comparing the rotor phase-averaged hub loads between different conditions along with PIV measurements, the results revealed substantial variations in aerodynamic effects from the ship airwake on the azimuthal rotor hub loads.

METHODOLOGY

Facility

The experiments in this study were performed in the John J. Harper Wind Tunnel located at the Georgia Institute of Technology. The Harper tunnel is a low-speed closed-return tunnel with a rectangular test section that measures 2.34 m (7.67 ft) in width, 2.13 m (7 ft) in height, and 3.22 m (10.58 ft) in length. The test section was built with modularity and optical accessibility in mind, allowing flexibility for different test configurations and requirements. A custom-built test rig, as shown in Fig. 1, was mounted on top of a platform elevated 0.7 m (2.3 ft) above the tunnel floor. This raised the test articles closer to the center of the test section to reduce boundary effects and possible wall interference during experiments. A three-axis servo-motor-driven linear traverse system with position-tracking magnetic encoders was installed on top of the elevated platform, downstream of the ship. This allowed precise control and tracking of the spatial position and velocity of the rotor model relative to the ship model.

Due to the substantial blockage from the setup, especially when the ship was yawed to higher angles, the freestream dynamic



Figure 1. Test rig set up in the tunnel test section.

pressure was corrected using the relation introduced by Barlow et al. (Ref. 22). Because the ship model and the rotor traverse were complex geometries and not aerodynamically shaped, solid and wake blockage corrections were estimated jointly to obtain the corrected dynamic pressure (q_c) shown in the following equation:

$$q_c = q_u \left(1 + \frac{1}{2} \frac{A_f}{A_t} \right) \quad (1)$$

where q_u is the uncorrected dynamic pressure directly measured through a pitot-static probe upstream of the models, A_f is the frontal area of the test setup, and A_t is the cross-sectional area of an empty tunnel test section. In this study, A_f consists of the frontal area of the models and the entire rotor traverse system. For A_t , the area considered was the cross-sectional area of the test section that was above the elevated platform. The increase in dynamic pressure varied based on the ship yaw angle (Ψ), or equivalently, the WOD angle. The estimated increase ranged from 4.8 to 6.4% with the ship yawed from 0 to 30 degs. This correction was applied to the reference velocity calculations throughout this paper.

Ship – The NATO Generic Destroyer

The ship model used was a 1:100 scale NATO-GD (Fig. 2) manufactured through additive manufacturing with polylactic acid (PLA). Surface pressures on the landing deck and hangar wall were measured through 126 pressure taps (98 on the landing deck and 28 on the hangar wall) connected to two 64-channel differential pressure scanners from Surrey Sensors (± 160 Pa full-scale range; 14-bit resolution; uncertainty $\pm 0.25\%$ full-scale). The interior of the ship model was made with an internal cavity and access panels to house the instrumentation for pressure measurements. Housing the pressure scanners inside the model minimized the pressure tube length between the surface taps and the sensor module, ensuring adequate response characteristics.

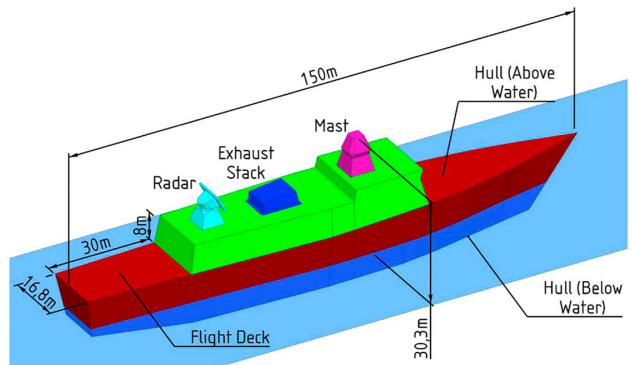


Figure 2. The full-scale NATO Generic Destroyer (Ref. 5).

To adjust the ship yaw angle, screw holes were embedded into the elevated platform as mounting points to fix the ship model at yaw angles up to 60 degs with 5-deg increments in both directions. These mounting points were located in such a way that the ship rotated about the center of the ship deck, fixing the center of the deck on the elevated platform even when yawed.

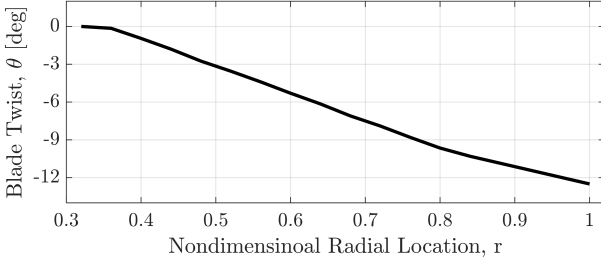


Figure 3. Rotor blade twist profile.

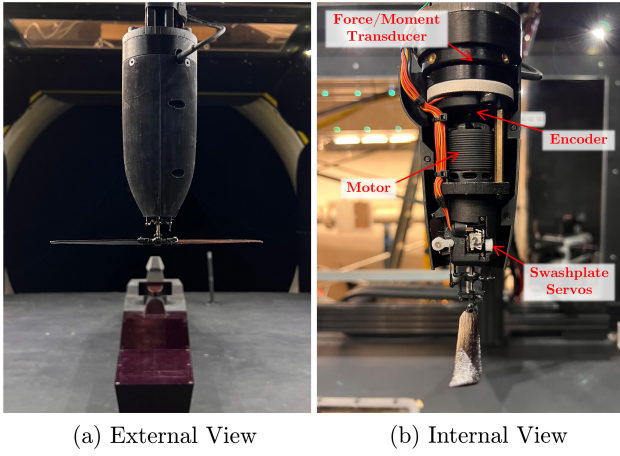


Figure 4. The rotor assembly.

Rotor – The NATO Generic Rotorcraft

In conjunction with the NATO-GD, the full-scale reference rotorcraft chosen in this study was the NATO Generic Rotorcraft (GR), which is a notional rotorcraft defined by the NATO AVT-315 group (Ref. 23). It was derived from the SH-60 Seahawk helicopter with similar dimensions. The cross-section of the main rotor blade has a NACA0012 airfoil, with a constant chord length of 0.53 m (1.73 ft) and a twist profile shown in Fig. 3.

The model rotor hub (Fig. 4) was a modified commercial off-the-shelf two-bladed radio-controlled helicopter with a fully servo-controlled swashplate assembly providing both collective and cyclic controls to the rotor. The rotor blades were custom made with carbon fiber reinforced polymer to match the geometry, airfoil, and twist profile of the NATO-GR. Note that the NATO-GR has a four-bladed rotor system, thus, the chord length of the model rotor blades was doubled to match the rotor solidity (σ). The rotor was driven by a T-motor AS2317 KV1250 brushless DC motor through an electronic speed controller (ESC) and a 12-volt power supply.

A magnetic rotary encoder with a angular resolution of 8196 counts per revolution was installed behind the brushless motor to track the rotor azimuthal position, enabling phase-correlated measurements. The entire assembly was attached to a Nano43 six-component force/moment transducer from ATI Industrial Automation for rotor hub load measurements. The calibrated range and uncertainty of the transducer are provided by the manufacturer and are listed in Table 1.

Table 1. Calibrated range and uncertainty of the Nano43.

	Range	Uncertainty (95% CI)
F_x, F_y, F_z	18 N (4.05 lbf)	1.25%
M_x, M_y, M_z	25 N·cm (2.21 lbf-in)	1.25%

A 3D-printed shroud was mounted to enclose the rotor assembly, leaving only the rotor hub exposed to the freestream, which prevented the undesired aerodynamic forces and moments of the rotor support structure, including the driving motor, from being measured by the transducer. The voltage signals from the transducer were amplified through an interface and power supply unit (IFPS) and sampled through a dSPACE MicroLabBox with 16-bit resolution.

The rotor angular rate and swashplate trim control were also integrated into the dSPACE system. The rotor angular rate was maintained through a proportional-integral-derivative (PID) controller, which used the median-filtered signal from the rotary encoder on the rotor assembly as the input and output a pulse-width modulation (PWM) signal to the ESC of the brushless motor. Trimming the rotor was accomplished through an auto-trim function based on a PID controller also using a median-filtered load measurements as the input. The trim controller was designed to maintain the target thrust (T) value and zero rolling and pitching moments (M_x, M_y) by manipulating the collective and cyclic controls of the swashplate.

Model Scaling

Table 2 lists the comparison of velocities, geometric dimensions, and scaling parameters between the full scale and model scale. The gross weight of the NATO-GR at full scale is 9,000 kg (19,842 lbs), which is approximately 90% of the maximum gross weight of the Seahawk helicopter. However, matching all dimensionless parameters in a model-scale wind

Table 2. Test conditions and scaling parameters.

	Full Scale Reference Condition	1:100 Model Scale
U_∞	40 kts (20.6 m/s)	5 m/s
l_s	150 m	1.5 m
w_s	22.1 m	0.221 m
Re_s	3.1×10^7	7.6×10^4
R	8.2 m	0.082 m
c	0.527 m	0.010 m
σ	0.08	0.08
Ω	27.0 rad/s (258 RPM)	656.5 rad/s (6,269 RPM)
M_{tip}	0.64	0.16
Re_{tip}	8.0×10^6	1.94×10^4
μ		0.093
C_T	0.0075 (Out-of-ground-effect)	

tunnel experiment is difficult. Thus, a compromise was made by only matching rotor μ and C_T , but not the Reynolds number of the ship, Re_s . This was done because it has been shown in several studies (Refs. 24,25) that a ship airwake was essentially insensitive to Reynolds number at a sufficiently high Reynolds number due to the nature of its bluff body with sharp edges. In these studies, it was observed that this Reynolds number insensitivity was true above a ship beam Reynolds number in the range of 10^4 to 10^5 . It was also demonstrated by Palm et al. (Ref. 6) that the NATO-GD was insensitive to Reynolds number above $Re_s = 4.5 \times 10^4$.

In this present study, the test condition resulted in a Re_s of 7.6×10^4 , which provided confidence that, although the Reynolds number was not matched, the characteristics of the airwake produced by the ship were similar to that in full scale. Additionally, the rotor solidity (σ) was of similar magnitude, giving a similar rotor blade loading coefficient (C_T/σ). However, the blade-tip conditions, M_{tip} and Re_{tip} , of the model were not possible to match the full-scale reference due to physical limitations at such a small scale. Therefore, one should keep in mind that the compressibility effects close to the tip of the rotor were likely not accurately scaled.

Particle Image Velocimetry

Flow field measurements were conducted using stereoscopic particle image velocimetry (SPIV). Two configurations were employed to measure the velocity fields: one for the horizontal rotor outflow plane and another for the streamwise-vertical planes (hereinafter referred to as “vertical planes”). Both setups utilized a Photonics DM30-527-DH Nd:YLF dual-cavity pulsed laser (527 nm, 30 mJ/pulse) with pulse separation times of 50 μ s for the rotor outflow and 150 μ s for the vertical plane measurements. Adjustable sheet optics with cylindrical lenses of focal length $f = -20$ mm were used to generate the laser sheet, resulting in a 10-degree divergence angle and a waist thickness of approximately 2 mm at the landing deck. Seeding particles with a nominal diameter of 4 μ m were produced using a Rosco Vapour fog generator with Rosco Fog Fluid (propylene glycol).

Figure 5 shows the laser illuminating a vertical sheet over the landing deck. Note that there was a laser sheet generated from

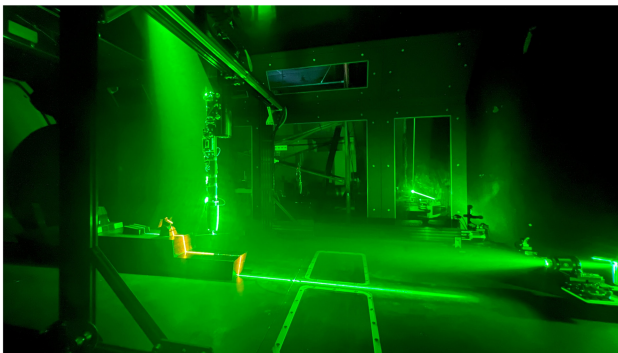


Figure 5. Laser illumination of the ship deck using two laser beams.

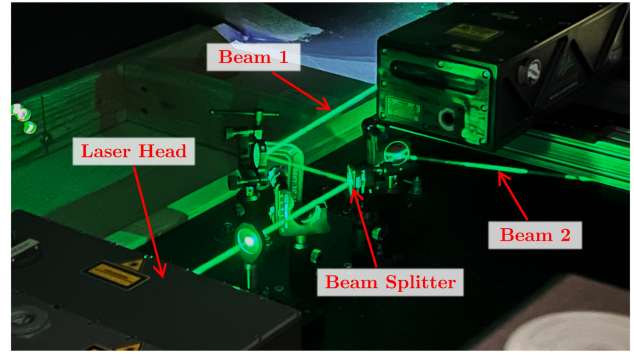


Figure 6. Optics setup for laser beam-splitting.

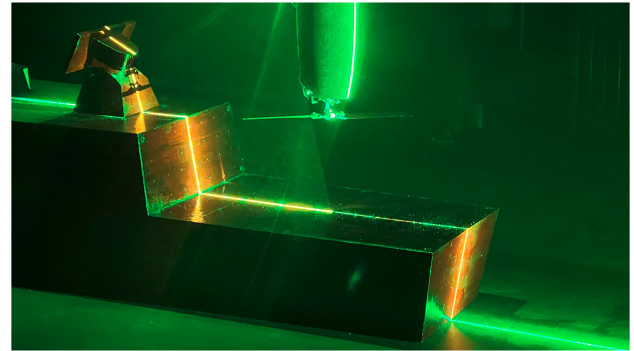
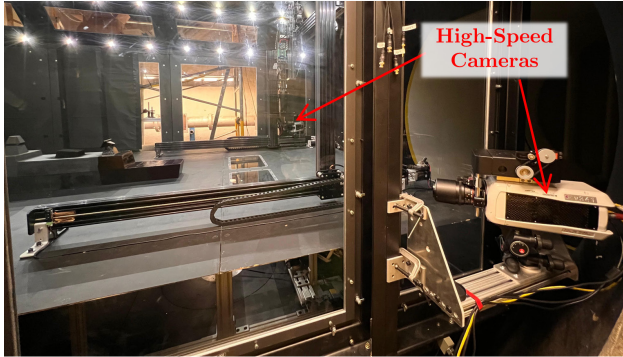


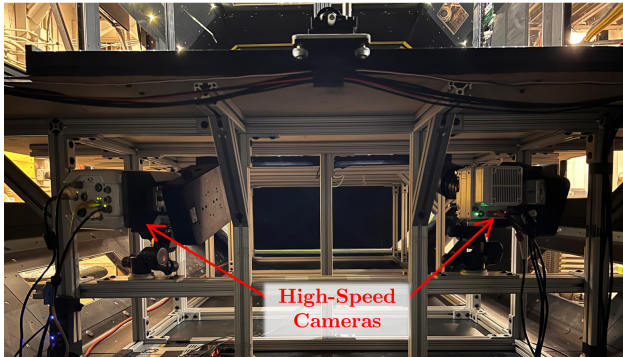
Figure 7. Close-up view of the fluorescent surface coating emitting orange light on ship deck.

the downstream side of the ship and another one from above the ship. To generate two laser sheets from different directions, the initial laser beam emitted from the laser head was split into two beams with a 50:50 beam splitter, as shown in Fig. 6, and routed through a series of mirrors. These two laser sheets were carefully aligned such that they coincided and formed one single sheet above the ship deck. This technique was adopted to avoid optical blockage caused by the support structure above the rotor when measuring near the rotor hub, with each sheet complementing the other in the blocked regions.

Additionally, the ship model surfaces around the deck region were coated with an acrylic-based fluorescent paint mixed with Kiton Red 620 (KR620), also known as Sulforhodamine B, as seen in Fig. 7. The KR620 dye has a maximum excitation and emission wavelength of approximately 560 and 580 nm, hence emitting orange light. According to the safety data sheet (Ref. 26), KR620 is a low-hazard dye compared with other commonly used dyes such as Rhodamine 6G (Ref. 27) and Rhodamine B (Ref. 28). KR620 has previously been used by Petrosky et al. (Ref. 29) to create dye-doped seeding particles for PIV measurements. By equipping the camera lens with a longpass filter, this technique was able to significantly reduce laser light reflections affecting the particle images near boundaries by only allowing the fluorescent light from the particles to pass through. However, in this present study, instead of using fluorescent particles, the dye was applied to the model surface as mentioned earlier. Thus, bandpass filters centered at 527 nm with a 20 nm bandwidth were mounted on the cameras to filter out the dye-emitted light. This approach



(a) Vertical Plane Configuration



(b) Horizontal Plane Configuration

Figure 8. PIV camera arrangements for the two different laser plane configurations.

was selected because containing the dye-doped particles within the large wind tunnel is challenging, and contamination of the tunnel circuit must be avoided.

In the vertical plane configuration, two Phantom high-speed complementary metal-oxide-semiconductor (CMOS) cameras ($2,560 \times 1,600$ pixels full resolution, $10 \mu\text{m}$ pixel size) from Vision Research were used to capture high-speed time-resolved images, as shown in Fig. 8(a). The cameras were equipped with 100 mm lenses with an aperture of $T/3.1$. A reduced resolution ($2,560 \times 1,060$ pixels) was used in this study to extend the data acquisition period that was limited by the onboard memory, which in turn captured more revolutions of the rotor while retaining most of the region of interest.

For the rotor outflow measurement configuration, a horizontal laser sheet was placed 4 mm ($\approx 0.05R$) below the rotor disk. Again, two Phantom high-speed cameras with the same pixel resolution as mentioned previously, which operated at full spatial resolution, were mounted below the elevated platform, viewing through a pair of windows, as shown in Fig. 8(b). The cameras were fitted with 135 mm lenses with an aperture of $T/2.2$. The laser and cameras were controlled and triggered synchronously through a programmable timing unit (PTU). Furthermore, the laser sheet optics for the vertical plane configuration were both mounted on lateral traverses, and a motorized focus control system was integrated into the camera lenses such that the measurement plane could be easily and remotely adjusted laterally from the control room.

Acquired image pairs were processed using the DaVis

10.2 software by LaVision Inc. The process started with a background removal algorithm to eliminate both static and unsteady reflections caused by spinning blades in the image background. The background-subtracted images were processed using a standard multi-pass cross-correlation algorithm with an initial interrogation window of 64×64 pixels with 50% overlap, and a final window size of 32×32 pixels with 75% overlap. A universal outlier detection algorithm with a filter size of 5×5 vectors was used during processing to iteratively detect and remove spurious velocity vectors. Regions that were blocked by the ship, rotor, or with substantial light reflections were masked out and were not used for vector calculations. This resulted in a vector spacing of 0.76 mm for the horizontal plane. For the vertical planes, the vector spacing varied slightly between measurement planes, depending on the position of the laser plane relative to the cameras, with an average spacing of 1.25 mm.

Test Matrix and Procedure

The test matrix in this study consisted of a stationary rotor force and moment survey across a grid of fixed locations at and around the landing deck for various WOD angles. An additional PIV investigation with the two different optical setups discussed previously was conducted for the rotor hovering above the landing deck at various locations and different WOD angles. All studies were conducted concurrently with the ship deck surface pressure measurements.

During the rotor force and moment survey, the position of the rotor hub was moved across a grid of hovering locations fixed to the ship body frame at $h = 1.16R$ above the landing deck behind the ship superstructure. Figure 9 illustrates the grid of surveyed hovering locations. Note that some locations closer to the edges were skipped at higher WOD angles due to limitations of the traverse travel ranges. Table 3 shows the extent of the survey including ship WOD angles, hovering height, and the number of grid points.

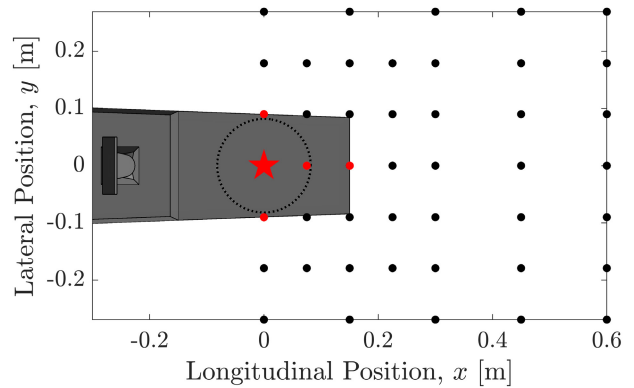


Figure 9. Ship-fixed grid survey points of the rotor hub behind the ship with red markers indicating location where PIV measurements were taken. (The star symbol denotes the HOD position. The dotted circle shows the size of the rotor disk at HOD.)

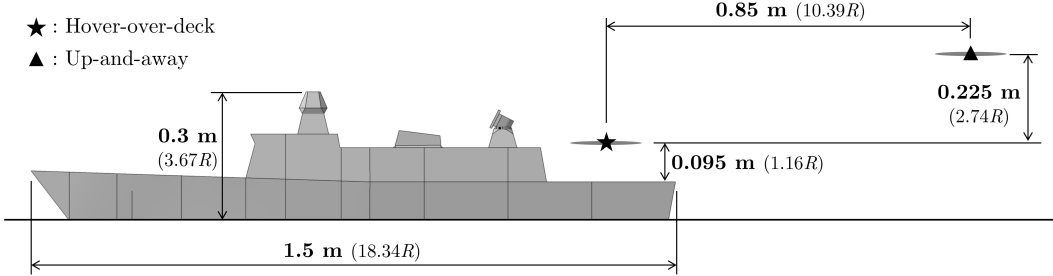


Figure 10. Relative position of the rotor hover-over-deck and up-and-away positions.

Table 3. Test matrix for the force and moment survey.

Rotor height above deck (h)	WOD angle (Ψ)	No. of grid points
1.16R (h_{HOD})	0	45
	G15, R15	44
	G30, R30	41

Prior to starting each test condition, the ship was manually adjusted to the yaw angles corresponding to the desired Green (G) or Red (R) WOD angles¹. Before each survey, the rotor was first trimmed to the desired thrust and zero in-plane moments at an up-and-away position at the target wind speed, which minimized the influence of the ship airwake on the rotor trim. Figure 10 illustrates the relative distances between the hover-over-deck (HOD) and up-and-away positions. Load measurements were taken at this location to serve as a baseline condition for each test run. Table 4 lists the statistics of the trimmed results of rotor hub loads at the up-and-away position for all measurements taken. The rotor trim control inputs to the swashplate servos were then held constant throughout the run. Data acquisition of loads and pressures were sampled at 12 kHz and 800 Hz respectively, and were triggered simultaneously after a 15-s settling period once the rotor reached each target position. 10 s of data were acquired at each position in order to capture sufficient cycles of the low-frequency content while keeping the duration of the experiment within the scheduled tunnel entry time frame. After each run, the rotor was returned to the up-and-away position, and a measurement was taken to ensure data consistency. A total of four survey runs were performed for each test condition to quantify the measurement uncertainties.

A similar procedure was used for the rotor PIV experiments. The rotor was first trimmed in the up-and-away position and brought to the target position while keeping the trim control inputs to the servos constant. Data acquisition was then initiated after a sufficient settling period of 15 s when the rotor had reached the target position. After each test run, the rotor was again traversed back to the up-and-away position

¹G, or Green, angles are wind conditions where the relative wind is blowing onto the deck from the starboard side of the ship. R, or Red, angles indicate the wind coming from the port side. For example, a G15 condition means that the freestream comes from a direction that is angled 15 degs to the right of the ship centerline, equivalent to a 15-deg ship yaw relative to the freestream.

Table 4. Statistics of mean rotor loads at the trimmed up-and-away condition.

	C_T ($\times 10^{-3}$)	C_{M_x} ($\times 10^{-5}$)	C_{M_y} ($\times 10^{-5}$)	\tilde{T}_{rms} (%)
Mean	7.37	9.96	-6.04	1.31
STD	0.06	7.22	6.58	0.15
Min-Max Range	1.46	1.63	1.71	0.4

for consistency checks. One single horizontal measurement plane located 4 mm ($\approx 0.05R$) below the rotor disk was used for the rotor outflow study. Double-frame images pairs were obtained at 400 Hz over 3.5 s, resulting in a total number of 1,400 flow realizations per test condition. For the vertical plane configuration, three separate measurement planes were used for each hovering condition, one through the center of the rotor and one on either side of the rotor, approximately 0.5R from the rotor hub. A total of 2,000 vector fields sampled at 400 Hz were obtained over 5 s for each test.

RESULTS AND DISCUSSION

Time-Averaged Rotor Hub Loads

Before delving into the rotor phase-averaged measurements, the time-averaged rotor hub loads with the rotor hovering at different locations around the landing deck were first examined. Figure 11 shows the contour maps of the change in mean thrust coefficient (C_T), unsteady root-mean-square (RMS) thrust (\tilde{T}_{rms}), rolling moment coefficient (C_{M_x}), and pitching moment coefficient (C_{M_y}) with the rotor hovering at the HOD height (h_{HOD}) above the landing deck compared with that measured in the up-and-away position under a headwind condition.

The unsteady RMS thrust was first defined by Lee and Zan (Ref. 8) and was calculated by integrating the unsteady components of the PSD spectra at full scale within the closed-loop pilot response frequency range (i.e., 0.2–2 Hz). It has previously been shown by McRuer (Ref. 30) that the responses within this frequency range pose a significant challenge to helicopter pilots. This accounts for the fact that higher-frequency fluctuations do not affect the handling qualities of the vehicle significantly, and at the lower frequencies, pilots can compensate through manual controls relatively easily. It also has been shown experimentally by

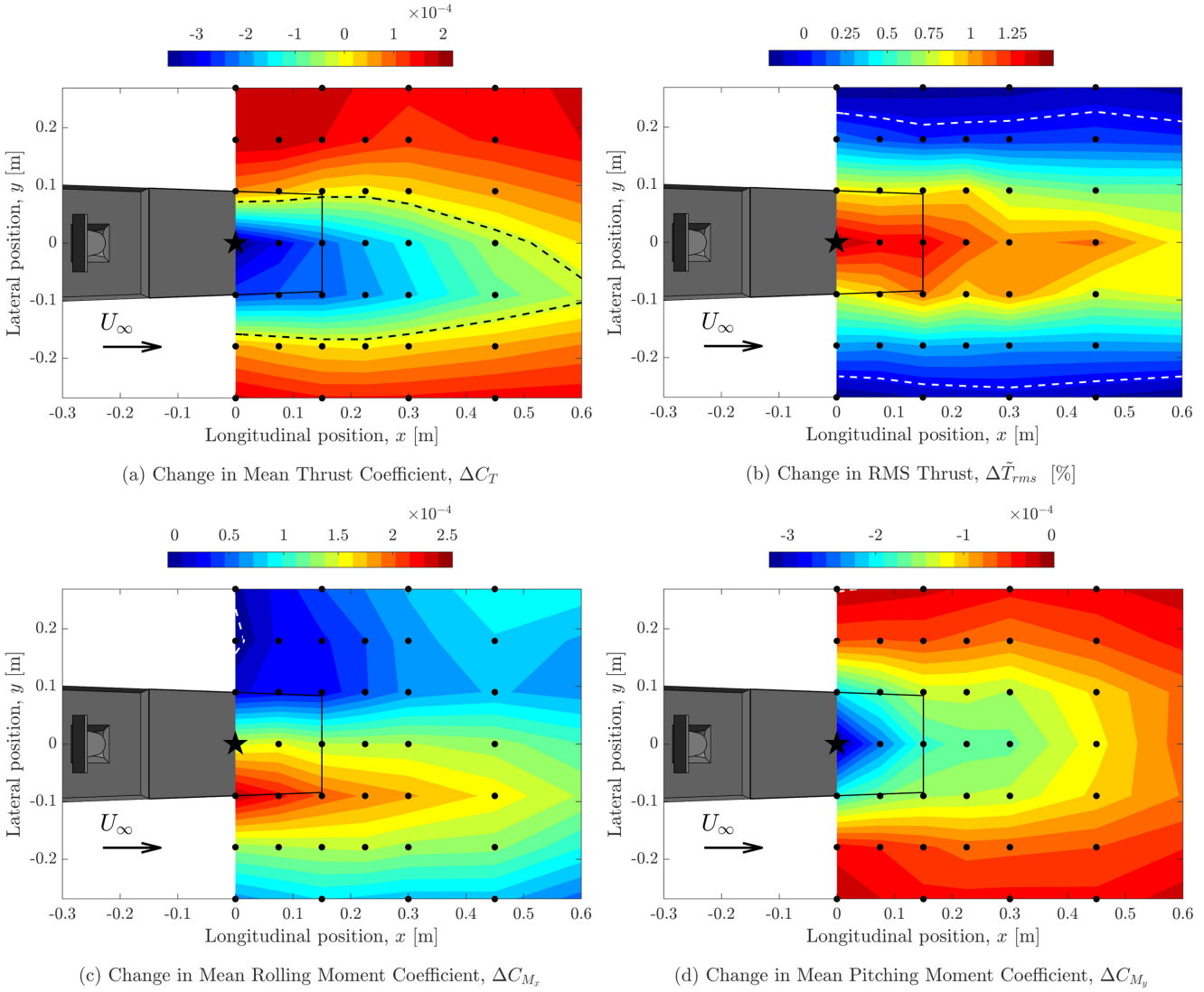


Figure 11. Change in the time-averaged rotor hub loads compared with the up-and-away measurements under a headwind condition. (Dashed lines indicate zero crossings.)

McTavish et al. (Ref. 31) that there was a positive correlation between the normalized unsteady RMS thrust within this frequency range in sub-scale experiments and the full-scale helicopter pilot workload. Note that, in sub-scale experiments, this frequency range was scaled by the ratio between the rotor angular rate of the scaled wind tunnel model and the full-scale reference. In this present study, this corresponded to a frequency range of 4.86–48.6 Hz,

From Fig. 11(a), one can see the rotor experience the greatest reduction in thrust at locations closest to the ship superstructure with a slight bias towards the port side of the ship. These locations also roughly coincide with the locations where the unsteady RMS thrust increased the most, as seen in Fig. 11(b). This was generally expected as the rotor was closely coupled with the unsteady ship airwake and recirculation behind the hangar wall when operating in these locations. In Fig. 11(c) and (d), the rolling moment showed a strong asymmetry about the ship centerline while the pitching moment exhibited a

more symmetric trend. Similar results were also obtained previously in experiments conducted by Chen and Rauleider (Ref. 21), which related this asymmetric effect to the rotational direction of the rotor causing the ship airwake to impinge on different sides (i.e., advancing and retreating) of the rotor when hovering at different locations. In this prior study, experiments were conducted with a slightly larger (+26%) rotor that had non-twisted rectangular blades. This suggests that, with rotors that had similar diameters to the width of the ship deck, these trends in time-averaged hub loads were generally consistent regardless of the dissimilarities in rotor blade geometry.

Phase-Averaged Rotor Thrust Under Headwind

Although rotor azimuth-correlated load measurements were available for all locations shown in Fig. 9, only the locations indicated by the red markers above the landing deck, where detailed PIV measurements were also taken, were chosen for this analysis. These locations were specifically chosen to

Table 5. Change in time-averaged rotor hub loads relative to up-and-away at positions of interest.

Position	ΔC_T ($\times 10^{-4}$)	ΔC_{M_x} ($\times 10^{-4}$)	ΔC_{M_y} ($\times 10^{-4}$)
Hover-over-Deck	-3.58	+1.55	-3.21
Aft 1/4 Ship Deck	-2.90	+1.61	-2.40
Stern	-2.26	+1.46	-1.76
Port	-2.47	+2.55	-1.82
Starboard	+0.93	+0.19	-1.99

demonstrate and examine how the lateral position (i.e., HOD, Port, and Starboard) and the longitudinal position (i.e., HOD, Aft 1/4 Ship Deck, and Stern) of the rotor hub caused different effects on the rotor-azimuth correlated hub loads. Table 5 lists the extracted values of ΔC_T , ΔC_{M_x} , and ΔC_{M_y} under headwind at these locations from Fig. 11 for reference. For brevity of the paper, only the rotor thrust component in the load measurements will be discussed in detail within the following sections.

The phase-averaged loads were calculated with a moving window of 5 deg, which was centered on every degree of rotor azimuth. Furthermore, in order to mitigate the inertial forces due to inherent mass imbalance and minor dissimilarities between the two rotor blades while interpreting the data, the 1/rev load components were filtered out during data processing. A set of sample data going through this filtering process is shown in Fig. 12. Instead of directly applying a

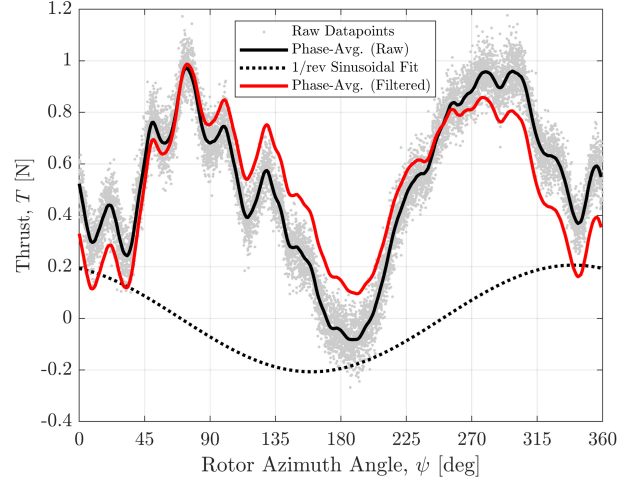


Figure 12. Sample thrust data of the 1/rev filtering process.

band-stop filter to the raw signals, the filtering was achieved by first taking the phase average of the raw data, i.e., going from gray dots to black solid curve, and then fitting the phase-averaged result with a 1/rev sinusoidal function (black dotted curve). A least-square method was used to obtain the amplitude and phase shift of this sinusoidal function. After retrieving the fitted coefficients, this function was then subtracted from the phase-averaged results to eliminate the 1/rev component and obtain the filtered result (red solid curve). Although this filtering technique minimized the fundamental 1/rev contribution of the imbalance, it should be noted that

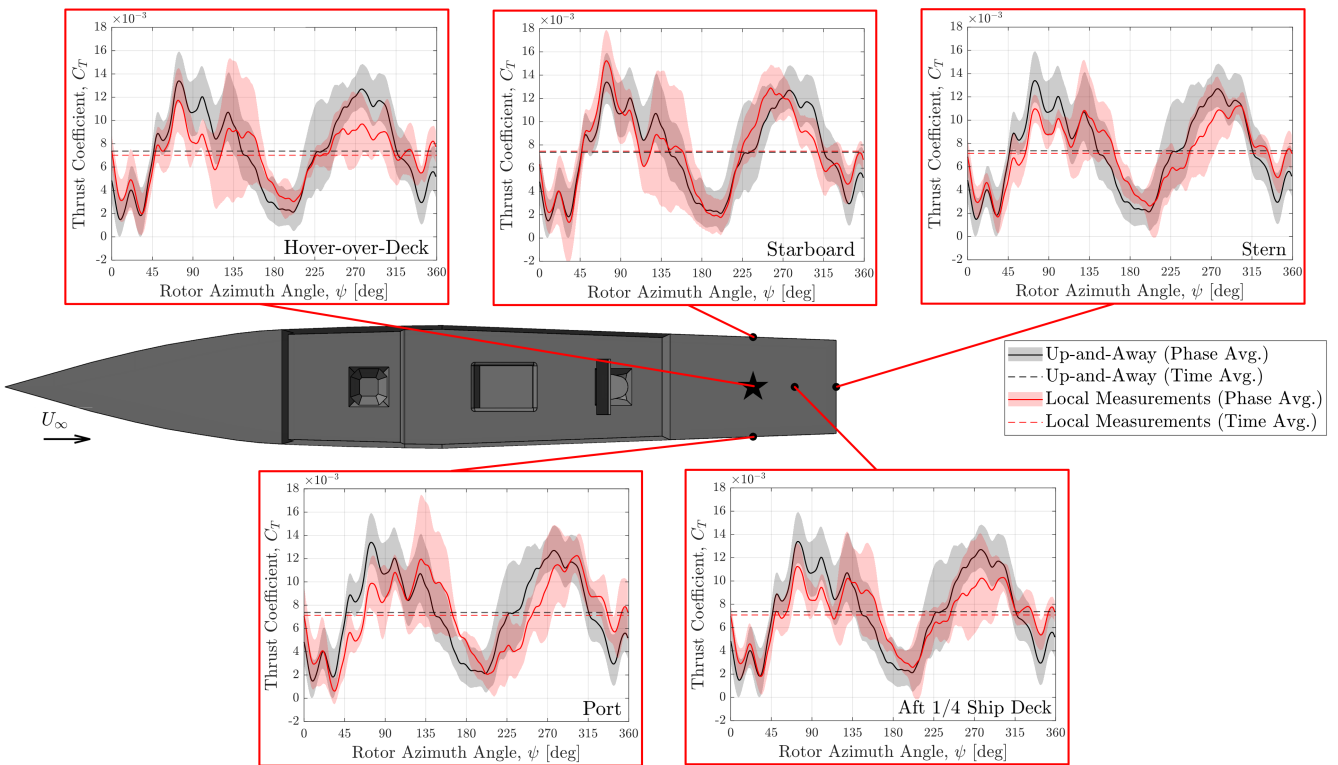


Figure 13. Rotor phase-averaged thrust coefficient at various hovering positions above the ship deck under a headwind condition. (Shaded areas indicate 95% confidence intervals.)

there might still be much weaker contributions from the higher harmonics that would be present in the results shown hereinafter.

Figure 13 shows the phase-averaged rotor thrust coefficient when hovering at these selected locations above the landing deck. The shaded areas indicate the 95% confidence interval over four repeatability runs using the Student's-t distribution. At each location, the measurement (red) was compared with the up-and-away condition (black). Since the rotor was a two-bladed rotor, all phase-averaged thrust exhibited a dominant 2/rev component with peaks occurring around an azimuth of 90 and 270 deg, where the blades experienced the highest benefit of translational lift on the advancing side from the incoming freestream velocity. However, due to the presence of the ship, the airwake flow structure behind the ship significantly altered the magnitude of thrust generated at different azimuth angles and showed clear dependencies on the hovering location above the ship landing deck.

To better assess and compare the effect of the ship airwake on the phase-correlated thrusts, the differences between the local and the up-and-away measurements were extracted for each hovering location and were split into two groups, longitudinal and lateral positions. Additionally, it was also assumed that the additional aerodynamic effects the ship airwake imposed on each of the rotor blades were similar, i.e., the changes in azimuthal thrust between 0 to 180 deg azimuth would be similar to those from 180 to 360 deg. Thus, these azimuth-correlated changes in loads that are presented in the following discussion were averaged both across 4 individual test runs and between the first and second half of rotor azimuth.

First looking at the change in azimuth-correlated thrust coefficient at the HOD position, as shown in Fig. 14 along with other longitudinal positions, there was a decrement in thrust generation between 35 and 140 deg azimuth, which corresponds to a blade orientation more perpendicular to the freestream flow. This mostly was contributed to by the reduction in freestream velocity due to the presence of the ship blockage, which affected the range of azimuth angles where it benefited most from translational lift.

For the rest of the azimuth angles, which corresponded to a blade orientation more parallel to the freestream, there was an increase in thrust coefficient lower in magnitude (-21%) compared with the thrust detriment discussed earlier. This is an interesting finding since one of the commonly accepted contributing factors to the reduction in thrust under the influence of the ship is the reingestion of the recirculatory flow behind the hangar wall. This slight increase in thrust when the rotor was near parallel with the freestream, with one of the blades being closest to the hangar wall, seems to contradict the above-mentioned reasoning. However, the reduced freestream due to the blockage of the ship, likely increased the effectiveness of ground effect, resulting in higher thrust. These combined effects suggested that the dominant contribution to the reduction in time-averaged thrust at the HOD position was the loss of translational lift.

Furthermore, as the rotor was moved downstream to the

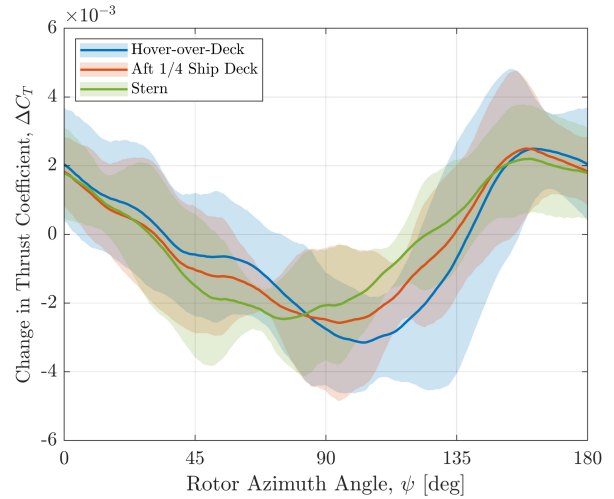


Figure 14. Comparison of the change in rotor phase-averaged thrust coefficient between different longitudinal hovering positions above the landing deck. (Shaded areas indicate 95% confidence interval.)

aft-quarter point of the landing deck and eventually further back to the stern, the magnitude of the increase in thrust stayed relatively constant irrespective of the longitudinal location of the hovering rotor. This once again indicates that the reingestion of the hangar wall recirculation was likely not dominant under these conditions. On the other hand, the severity of the thrust detriment reduced gradually along with the peak shifting to an earlier azimuth angle as the rotor was placed further back towards the stern, which partially regained the lost translational lift.

To visualize the rotor downwash distribution below the rotor, which could partially indicate the thrust production across the rotor disk with simple momentum theory, the PIV flow field measurements at the rotor outflow plane were examined. Since the measurement plane was slightly below the rotor disk, it is expected that the entire wake structure would have shifted downstream due to convection from the freestream. In order to correct for this shift, a fixed-wake convection model based on Taylor's hypothesis (Ref. 32) was applied, which was also employed by Deng et al. to reconstruct 3D spatial-temporal wakes of a flapping-wing micro air vehicle (Ref. 33), and also Chen and Rauleder (Ref. 21) to estimate the rotor inflow properties, where details of the correction process can be found.

Figure 15 shows the change in time-averaged downwash velocity normalized by the freestream velocity compared with the measurement performed with the rotor in isolation and out of ground effect, which is shown in Fig. 16. Due to the limitations of the experimental apparatus, conducting PIV measurements around the rotor at the up-and-away position was unachievable. Thus, a separate set of PIV measurements were conducted without the presence of the ship to serve as the reference condition. During these tests, the rotor was hovering and trimmed $4R$ above the ground where the center of the ship deck was located at.

Shown in Fig. 15(a), there was a clear increase in downwash

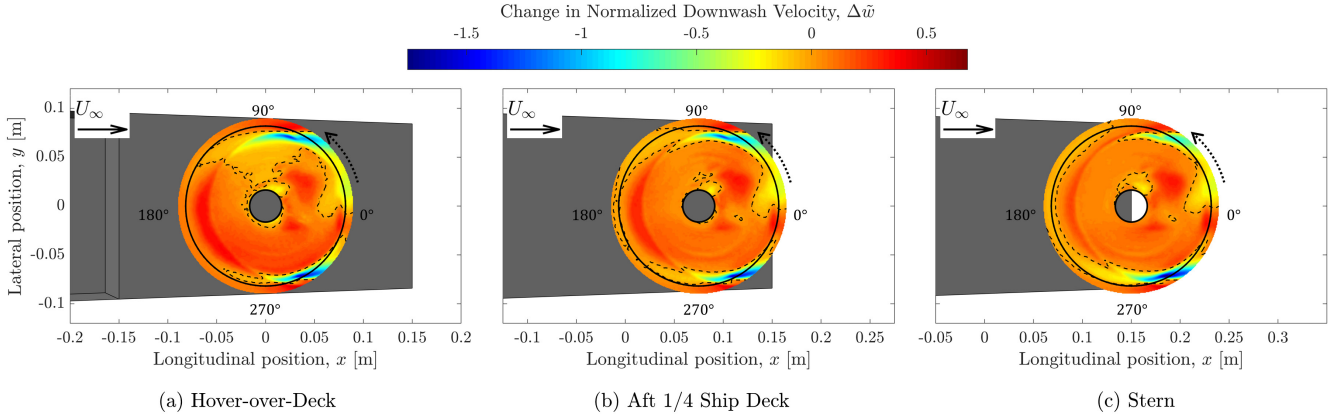


Figure 15. Change in normalized downwash velocity at $0.05R$ below rotor disk with the rotor hovering at various longitudinal locations above the landing deck compared with the rotor in isolation. (Black solid lines denote rotor disk and root cutout. Dashed lines indicate zero-crossings.)

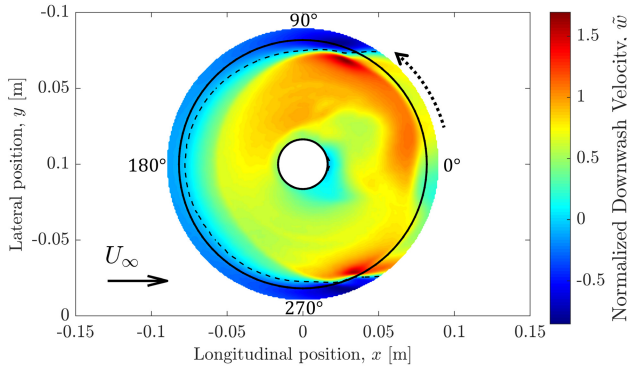


Figure 16. Normalized downwash velocity at $0.05R$ below rotor disk with the rotor in isolation and out of ground effect. (Black solid lines denote rotor disk and root cutout. Dashed lines indicate zero-crossings.)

velocity around the forward half of the rotor disk and a small region behind the hub as well; this corresponds to the increase in thrust presented earlier around 0 and 180 deg azimuth. Note that, at this azimuth angle, the forward-pointing blade would also experience some additional inflow due to the recirculation region behind the hangar wall, adding to the downwash measured here. Also, the rearward-pointing blade would experience some level of influence from the change in wake structures shed from the rotor supporting mount above. As the azimuth angle was increased, the advancing blade started to encounter the effect of reduced translational lift from the ship blockage, causing a reduction in downwash, while the retreating blade continued to generate similar level of increase in downwash compared with the undisturbed reference condition.

Around 90 deg rotor azimuth, the advancing blade experienced the most significant reduction in translational lift accompanied by the change in the interactions between the skewed tip vortices. At the same time, the retreating blade was experiencing the highest freestream velocity, and thus, the magnitude of increase in downwash reduced. The combined effect resulted in the thrust produced by the blades being the

lowest around this azimuth angle as shown in Fig. 14. Note that the peak in thrust detriment came slightly after 90 deg rotor azimuth, which could be due to the retreating blade interactions with the downstream-contracted tip vortices and the phase lag from the transient effect of the unsteady aerodynamic phenomenon.

As the rotor was positioned further aft on the ship deck, first toward the aft-quarter (Fig. 15(b)) and then near the stern (Fig. 15(c)), the region of downwash reduction on the advancing side of the rotor gradually diminished. This indicates that the advancing side was beginning to recover the translational lift it had previously lost, which corresponds to the slight reduction in thrust deficit observed near the 90 deg rotor azimuth in Fig. 14. Furthermore, the low downwash region caused by the interaction of tip vortices with the advancing blade shifted further downstream, behind the rotor disk. Combined with the increased freestream velocity experienced by the retreating blade on the upstream side, these effects led to a shift in the azimuth angle of minimum thrust toward a smaller angle as the rotor hovered further aft over the landing deck.

Next, the effect of lateral rotor positions on azimuthal thrust variation is shown in Fig. 17. Due to significant velocity gradients across the rotor disk, thrust variation across azimuth angles differed noticeably between lateral hover positions. When the rotor was positioned at the HOD location and on the port side of the landing deck, the azimuthal thrust variation exhibited a single peak, with the maximum thrust deficit occurring at offset azimuth angles. Flow interactions on the port side shifted this maximum thrust deficit forward by approximately 40 deg in azimuth relative to the hover-over-deck condition, greater than the shift observed when hovering near the stern. In contrast, the starboard-side hover position resulted in two distinct peaks, indicating that aerodynamic interactions in this region produce significantly different effects compared to other hover locations.

Again, a more detailed analysis can be conducted by examining the change in downwash velocity, relative to the isolated reference condition, beneath the rotor disk at two laterally

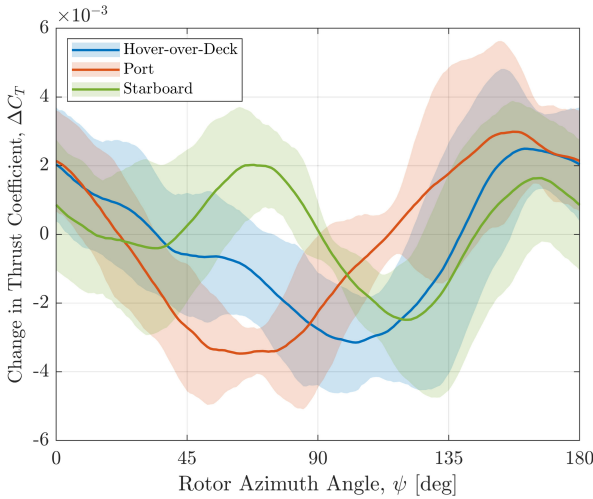


Figure 17. Comparison of the change in rotor phase-averaged thrust coefficient between different lateral hovering positions above the landing deck. (Shaded areas indicate 95% confidence intervals.)

offset hover positions, as shown in Fig. 18. This can be compared to the downwash distribution for the HOD condition presented earlier in Fig. 15(a), highlighting regions of increased and decreased downwash. Focusing first on the port side case (Fig. 18(b)), where similar thrust trends were observed with a shifted peak deficit compared to the HOD. The upwind portion of the retreating side exhibited a reduced downwash. This reduction is attributed to the accelerated freestream flow encountered outside of the ship deck, reducing thrust on the retreating blade. Additionally, decreased downwash between 0 and 90 deg azimuth contributed to an early onset of thrust reduction shortly after the 0/180 deg azimuth crossing. Following this early drop, a notable increase in downwash was observed between 90 and 180 deg azimuth. In this region, the downward flow induced by recirculation behind the hangar wall likely enhanced the inflow through this section of the rotor disk, contributing to a recovery in thrust beyond the 90 deg azimuth, despite potential impacts on the local blade angle of attack. Simultaneously, the retreating blade on the opposite side exited the freestream-affected region and began to regain thrust as well.

Turning to the starboard side hover condition, shown in Fig. 18(a), the most notable feature is the high downwash region shifting to the upstream half of the retreating side of the rotor. Here, the retreating blade experienced reduced freestream velocity and additional mass flow due to recirculation, leading to additional downwash velocities. Combined with a slight reduction in downwash just after 0 deg azimuth on the rear half of the rotor disk, this resulted in a near-neutral change in thrust initially, as shown in Fig. 17. Around 45 deg azimuth, the advancing blade began to generate higher downwash in a region that remained relatively unaffected by the ship airwake across all conditions analyzed; see Figs. 15 and 18. The combined effect of both blades contributed to a significant increase in thrust after crossing the 45 deg azimuth. However, immediately following this thrust peak, the retreating blade

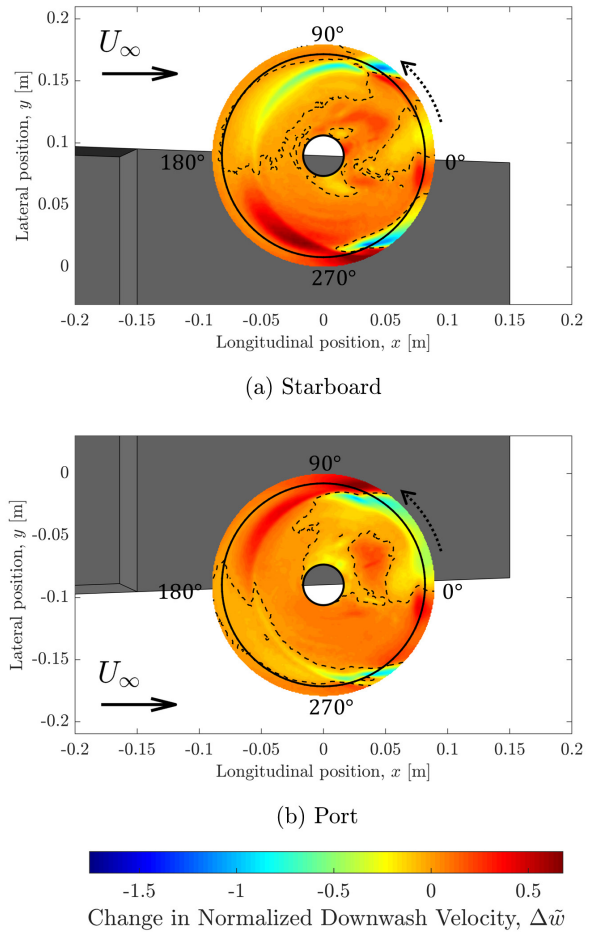


Figure 18. Change in normalized downwash velocity at 0.05R below rotor disk with the rotor hovering at various lateral locations above the landing deck compared with the rotor in isolation. (Black solid lines denote rotor disk and root cutout. Dashed lines indicate zero-crossings.)

began to lose the benefit of the low-speed airwake, while the advancing blade encountered greater influence from the faster freestream. This led to a counterintuitive reduction in downwash velocity, and consequently in thrust, likely due to a decrease in the local inflow angle and higher interactions with the tip vortices outweighing the benefit of increased local tangential velocity experienced by the advancing blade.

While downwash velocities measured below the rotor disk can provide insight into thrust production, interpreting them requires caution. Increased downwash does not always correspond to increased thrust; it may also result from higher inflow velocities induced by external disturbances, which can actually degrade thrust production. Therefore, to further support the findings discussed so far, a more rigorous analysis based on momentum conservation across the rotor disk was performed.

The rotor thrust can be expressed as the rate of change of vertical momentum across the rotor, or equivalently, as the mass flow rate perpendicular to the rotor disk (\dot{m}_z) multiplied by the change in vertical velocity (Δw_{disk}) across the disk,

integrated over the rotor disk area (A), as shown in Eq. 2:

$$T = \iint \Delta w_{disk} d\dot{m}_z = \iint \Delta w_{disk} \cdot (\rho \cdot w_{disk} \cdot dA), \quad (2)$$

assuming minimal momentum exchange through the sides of the rotor disk. The elemental thrust (dT) can then be expressed as:

$$dT = \rho \cdot w_{disk} \cdot (w_{outflow} - w_{inflow}) dA, \quad (3)$$

where w_{disk} , w_{inflow} , and $w_{outflow}$ are the vertical velocities at the rotor disk, just above the disk, and just below the disk, respectively. Assuming air density remained constant, a nondimensional thrust index (I_T) proportional to the local elemental thrust can be defined as:

$$dT \propto I_T = \tilde{w}_{disk} \cdot (\tilde{w}_{outflow} - \tilde{w}_{inflow}), \quad (4)$$

where velocities are normalized by the freestream velocity. Regions of higher I_T indicate areas of greater thrust production on the rotor disk.

However, direct measurements of inflow just above the disk from the horizontal-plane PIV setup were not possible due to optical blockage. As an alternative, vertical-plane PIV measurements were used to obtain the vertical velocity components. Velocities were extracted approximately $0.05R$ above and below the rotor plane to represent \tilde{w}_{inflow} and

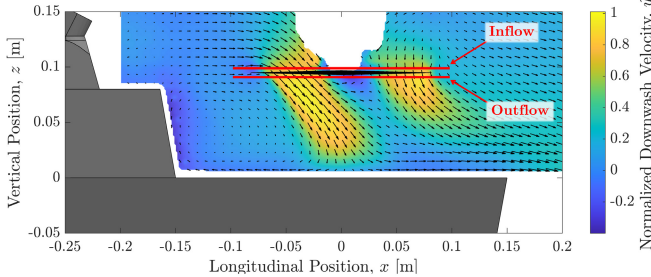


Figure 19. Time-averaged normalized downwash velocity measured at the center of the rotor hovering at the HOD position under headwind. Red lines indicate locations where the inflow and outflow velocity profiles were extracted for thrust estimation.

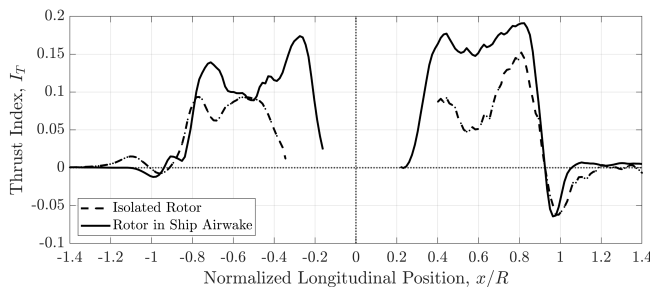


Figure 20. Profiles of thrust index (I_T) at the center of the rotor hovering at the HOD position under headwind compared with the isolated rotor.

$\tilde{w}_{outflow}$, respectively, as illustrated in the sample flow field in Fig. 19. \tilde{w}_{disk} was estimated using the mean between \tilde{w}_{inflow} and $\tilde{w}_{outflow}$. Using Eq. 4, thrust index profiles were calculated and are shown as solid lines in Fig. 20. It should be noted that solid blockage and reflections from the rotor support caused missing data in portions of the flow field, as seen in the blank region above the disk in Fig. 19, leading to corresponding gaps in the thrust index profiles.

Additionally, to evaluate the effects of the ship airwake, thrust index profiles were also extracted from vertical-plane PIV measurements of an isolated rotor in forward flight and out of ground effect, as mentioned previously. These are plotted as dash-dot lines in Fig. 20. From this measurement plane, corresponding to the 0/180 deg azimuthal positions, it was observed that both the upstream (negative x) and downstream (positive x) sides of the rotor disk exhibited higher thrust levels compared to the isolated case. This finding is consistent with previous observations from direct thrust measurements and horizontal-plane downwash measurements for the rotor hovering at the HOD location under a headwind condition.

To further investigate the cases discussed above and compare them with the isolated rotor measurements, velocity profiles and thrust indices were extracted at three lateral locations across the rotor disk: the centerline ($y = 0$), advancing side ($y = +0.5R$), and retreating side ($y = -0.5R$), as shown in Fig. 21, for qualitative assessment of thrust production across the rotor disk.

Focusing first on the HOD position in Fig. 21(b), it is evident that the ship airwake affected different quadrants of the rotor disk to varying degrees, consistent with the earlier observations from pure downwash analysis. Increased thrust was primarily observed on the rear half of the advancing side, as well as near the 0/180 deg azimuth along the centerline. Although some data near the forward half of the rotor disk were missing due to optical blockage, it is still apparent that the forward half of the advancing side produced less thrust under the influence of the ship airwake compared to the isolated rotor condition. Meanwhile, on the retreating side, changes in thrust were generally smaller and more localized, with slight variations attributed to modified interactions with the skewed tip vortices, particularly in the upstream regions. The combined effects seen from the thrust index profiles support the measured thrust trends of the HOD position shown in Fig. 14: an initial thrust increase around 0 deg azimuth, followed by a gradual reduction as the rotor approached 90 deg azimuth, reaching a minimum after passing 90 deg, where the advancing blade began to experience the greatest thrust loss.

As the rotor was repositioned further aft, first to the aft-quarter point on the landing deck (Fig. 21(d)) and then to the stern (Fig. 21(e)), only minor changes were observed in the upstream half of the rotor disk on both advancing and retreating sides. The recovered freestream velocity at the upstream edge led to slightly greater skewing of the tip vortices, marginally expanding the low-thrust region near the blade tips. However, a more pronounced thrust enhancement appeared on the rear half of the retreating side, which was an effect not clearly

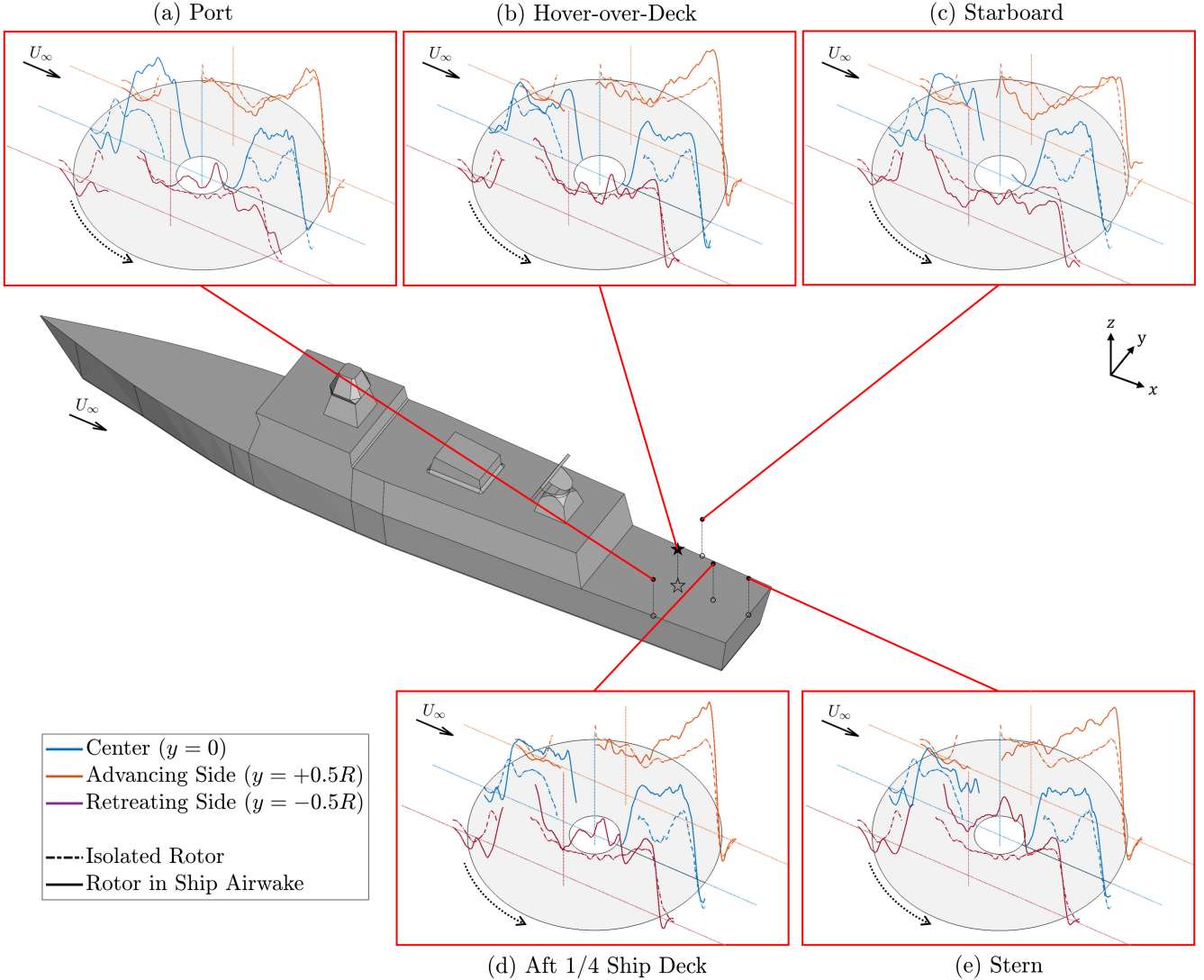


Figure 21. Profiles of thrust index (I_T) at various lateral locations on the rotor disk with the rotor hovering at different locations above the landing deck under headwind conditions compared with the isolated measurement.

captured by the earlier downwash analysis (Fig. 15(c)). This enhancement contributed to the earlier thrust recovery observed in the thrust measurements in Fig. 14. Although the changes in time-averaged thrust in Fig. 11(a) and Table 5 suggested a slow recovery towards the up-and-away condition, the thrust index profiles reveal more complex and localized beneficial and detrimental effects across the rotor disk.

Next, examining the lateral hover positions in Figs. 21(a) and (c), both port- and starboard-hoovering cases exhibited similar trends at 180 deg azimuth, where the accelerated flow along the sides of the ship reduced thrust at the upstream edge and also on the freestream-exposed side of the rotor, i.e., the advancing side for the starboard-hoovering case and the retreating side for the port-hoovering case. Interestingly, the rear half of the advancing side showed nearly neutral thrust changes relative to the isolated rotor in both conditions, despite the very different flow environments. Consequently, rotor thrust during early azimuth angles (between 0 and 90 deg)

became dominated by the performance of the retreating blade, where it was between 180 and 270 deg azimuth. During these azimuth angles, the port-hoover case exhibited a noticeable thrust reduction (Fig. 21(a)), while the starboard-hoover case showed small increases and decreases of similar magnitudes (Fig. 21(c)). This behavior led to an early thrust drop for the port-hoover case in Fig. 17, and a near-neutral thrust change at early azimuth angles for the starboard-hoover condition.

Overall, the analysis of thrust indices largely supports the phase-correlated trends observed in the directly measured rotor thrust. Additionally, it reveals several interaction phenomena at specific rotor azimuth angles that were not captured through the analysis with downwash measurements alone.

Phase-Averaged Rotor Thrust Under Various WOD Angles

This section analyzes the effects of ship WOD angles on the azimuthal variations in rotor thrust. Figure 22 presents

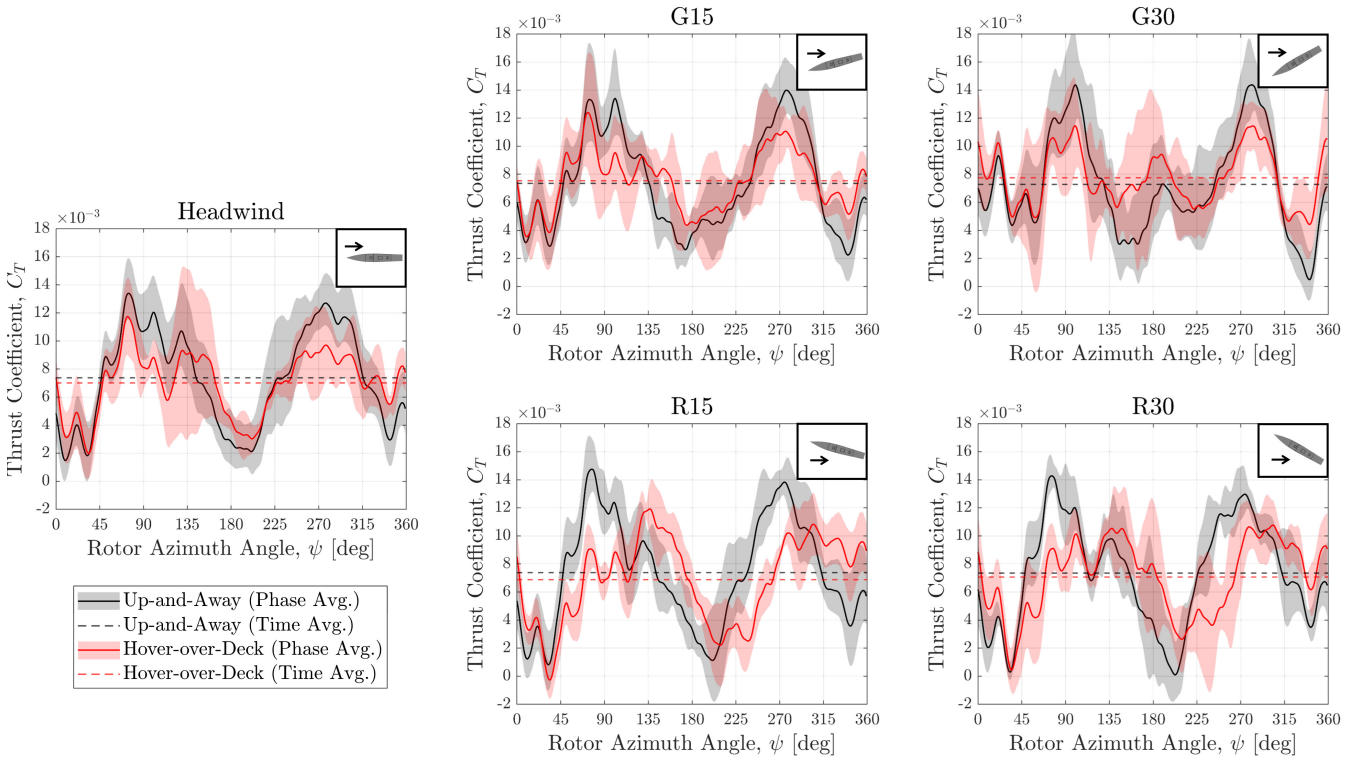


Figure 22. Rotor phase-averaged thrust coefficient under different WOD angles while hovering at the hover-over-deck position. (Shaded areas indicate 95% confidence intervals.)

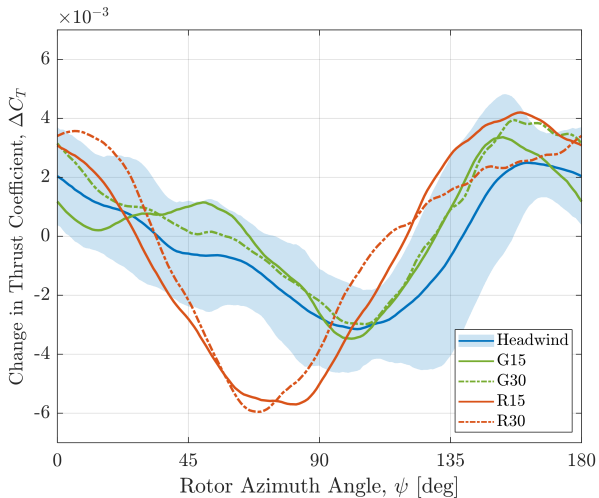


Figure 23. Comparison of the change in rotor phase-averaged thrust coefficient under different WOD angles while hovering at the hover-over-deck position. (Shaded area indicates headwind 95% confidence interval.)

the phase-averaged rotor thrust coefficient under headwind conditions, as well as with 15 and 30 deg winds from either side of the ship, with the rotor hovering at the HOD position. For reference, the corresponding up-and-away measurements for each WOD angle are included in the plots as well. It is noted that small variations exist between the phase-averaged up-and-away results across the different WOD cases. These

differences are likely due to minor changes in the rotor hub mechanism, such as wearing of the shaft and bearings, and slight discrepancies in up-and-away flow conditions, caused by the limited distance downstream from the influence of the ship airwake, which is an inherent limitation imposed by the length of the test section and traverse travel range. Nevertheless, despite these small differences in the trimmed up-and-away conditions, the aerodynamic impacts induced by the ship airwake, specifically the changes in rotor hub loads, should remain comparable across all cases.

As shown in Fig. 22, the rotor under green wind conditions exhibited similar beneficial and detrimental effects from the ship airwake at azimuthal positions consistent with those observed under headwind. In contrast, the aerodynamic effects under red wind conditions were more pronounced, not only reducing the time-averaged thrust but also shifting the apparent phase of azimuthal thrust variation. To better illustrate these differences, the change in phase-averaged thrust was computed using the same methodology, with results shown in Fig. 23. For clarity, only the 95% confidence interval of the headwind condition was plotted, though the uncertainty bands under all conditions were comparable to that of the headwind case.

From Fig. 23, the influence of different downstream wake structures due to wind directions becomes evident. All conditions generally exhibit a thrust increase around the 0/180 deg rotor azimuth, with red wind cases showing the greatest enhancement. Additionally, for the R30 case, the peak thrust increment lagged behind that of the R15 case by approximately 28 deg. Green wind conditions produced

results similar to headwind, with slightly higher thrust values observed around 45 and 135 deg azimuth. The most significant observation, however, is the maximum thrust deficit under red wind conditions, which occurred approximately 30 to 40 deg earlier in azimuth compared to the headwind and green wind cases. The magnitude of this thrust reduction was the largest among all conditions studied thus far, including those presented in Figs. 14 and 17. This suggests that portions of the retreating rotor blades may have experienced localized stall due to highly unsteady flow interactions at these azimuthal angles under red wind conditions.

Once again, downwash velocities directly beneath the rotor disk ($0.05R$) were compared across different WOD angles, using the isolated rotor condition previously shown in Fig. 16 as a baseline reference. Starting with the green wind cases shown in Figs. 24(a) and (b), an initial observation suggests that the advancing blade may have produced less thrust, indicated by a broader region of reduced downwash that even extends beyond 180 deg azimuth. However, the thrust measurements shown in Fig. 23 do not reveal a corresponding

loss in thrust compared to the headwind case. Instead, a slight positive effect was seen. This suggests that the retreating blade on the opposite side may have generated higher thrust, compensating for the reduction on the advancing side. To verify this, the thrust index analysis introduced earlier was applied, which will be discussed later alongside other WOD conditions.

On the other hand, under the red wind conditions shown in Figs. 24(c) and (d), the airwake from the ship superstructure also had a strong detrimental effect on the advancing side, particularly towards the outer portion of the disk. This led to a substantial reduction in downwash velocity from 0 deg up to approximately 120 deg azimuth. On the retreating side, a reduction in downwash, similar to that on the advancing side in the green wind conditions, persisted due to the exposure to the faster freestream. The retreating blade, typically operating at a higher angle of attack, may have experienced localized stall due to added unsteadiness from the roll-up flow over the windward edge of the ship deck and increased interactions with tip vortices. It is important to note that the model-scale

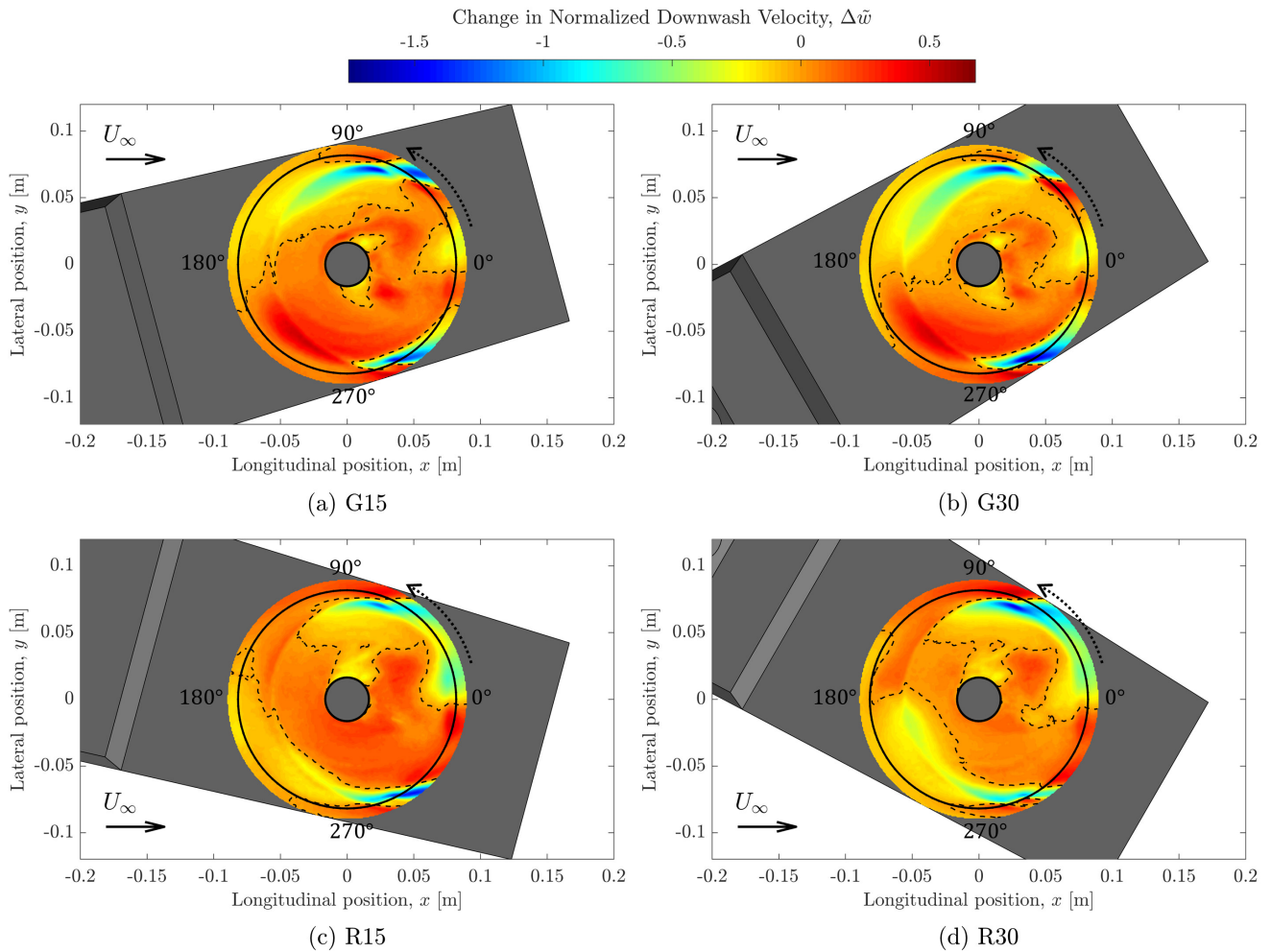


Figure 24. Change in normalized downwash velocity at $0.05R$ below rotor disk under different WOD angles while hovering at the hover-over-deck position compared with the rotor in isolation. (Black solid lines denote rotor disk and root cutout. Dashed lines indicate zero-crossings.)

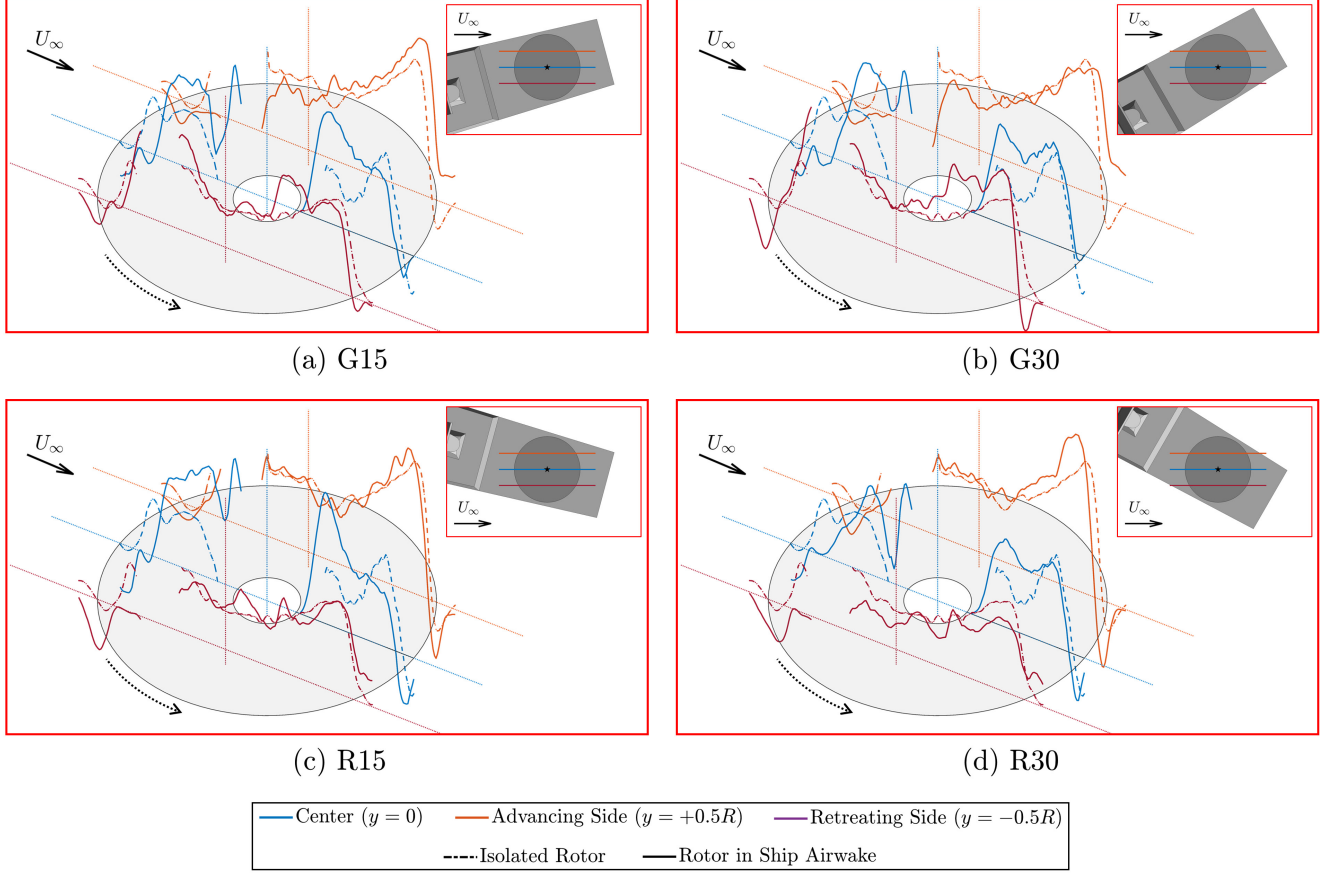


Figure 25. Profiles of thrust index (I_T) at various lateral locations on the rotor disk with the rotor hovering at the HOD position under different WOD angles compared with the isolated measurement.

Reynolds number was approximately two orders of magnitude lower than full scale, making the scaled rotor blades more susceptible to early stall onset. Together with the advancing blade thrust reduction, this likely contributed to the pronounced thrust deficit observed under red wind conditions.

Next, analyses of the thrust index were performed to further investigate thrust performance across azimuth angles. Starting with the green wind conditions in Figs. 25(a) and (b), the thrust index profile confirms that the forward half of the advancing side suffered a negative impact due to the higher freestream velocity blowing over the windward deck edge. This reduction in thrust grew more severe as the WOD angle increased. However, on the opposite side across the rotor disk, the retreating blade showed noticeable increase in thrust as the WOD angle was increased. This resulted in a net positive effect of a relative to the headwind case after 90 deg azimuth. Moreover, based on Fig. 23, the thrust performance of the rotor at early azimuth angles under green winds appeared to be similar to the headwind condition. However, closer inspection of the thrust index profiles (Figs. 25(a) and (b)), compared against the headwind case (Fig. 21(b)), reveals that the rotor was operating in a significantly different aerodynamic state under quartering winds. In early azimuth angles, the downstream section of the advancing side produced substantially less thrust, approaching levels seen with

the isolated rotor. This was counteracted by the notable thrust increase on the upstream half of the retreating side, resulting in similar combined thrust from both blades as seen in Fig. 23.

Moving to the red wind conditions shown in Figs. 25(c) and (d), it is interesting to note that the downstream half of the advancing side performed similarly to the green wind conditions, despite the advancing blade being fully immersed in the airwake of the ship superstructure in the red wind case and more exposed to freestream flow under green wind conditions. However, the retreating blade showed a significant thrust reduction under red winds, greater than that seen on the advancing side under green winds, likely due to the increased unsteady interactions leading to localized blade stall. As a result, the combined thrust from both blades showed a sharp drop at early azimuth angles, as shown in Fig. 23. Once the rotor passed 90 deg azimuth, the advancing blade entered the upstream half of the disk, where thrust indices for both R15 and R30 conditions recovered to values similar to the isolated rotor case, and significantly higher than under a headwind. This contributed to the rapid thrust recovery that eventually exceeded all other wind angles, as seen in Fig. 23.

Although the thrust indices extracted from vertical-plane PIV measurements provide strong support for the trends observed in the directly measured thrust from the force/moment transducer,

the limited lateral spatial resolution of the measurements still offers only a partial view of the interactional aerodynamic phenomena across the entire rotor disk. Therefore, caution should be exercised when interpreting these specific results.

CONCLUSIONS

This study revealed how the complex interaction between a rotor and the unsteady ship airwake significantly alters both the time-averaged and, more importantly, the phase-averaged rotor thrust characteristics while hovering above or near the ship deck of a NATO-GD. Time-averaged measurements indicated the most severe thrust reduction and increased unsteady loading when the rotor was positioned closest to the ship superstructure. These effects are attributed to a combination of ground effect, loss of translational lift due to ship blockage, and localized recirculatory flow, which also induced asymmetries in rolling and pitching moments. Additionally, these trends were consistent with prior experimental observations using different rotor geometries, suggesting a generalizable aerodynamic behavior in shipboard hover conditions.

Phase-averaged thrust analyses provided deeper insight into the ship-airwake-rotor aerodynamic interactions by revealing location-dependent variations in thrust generation across the rotor disk. At the HOD and other longitudinal positions along the centerline of the deck, translational lift losses likely dominated the thrust deficit near 90 deg azimuth, while lateral displacements of the rotor introduced complex asymmetries driven by freestream velocity gradients and flow structures behind the ship superstructure. Downwash distributions and the thrust estimation through thrust index from PIV studies supported these findings, linking thrust changes to flow phenomena at specific azimuth angles such as increased vortex interactions and localized rotor downwash variations.

When considering different WOD angles, the rotor hovering at the HOD position exhibited distinct shifts in azimuthal thrust caused by changes in the influence from the ship airwake. Under port-side wind conditions, localized stall and unsteady flow interactions led to pronounced thrust reductions, particularly on the retreating blade. Meanwhile, starboard wind conditions resulted in more “balanced” effects, with thrust increases on the retreating side compensating for losses on the advancing side. These findings suggest that the aerodynamic performance and loads on the rotor are highly dependent on the specific WOD angle, and that the interactions between ship airwake and rotor blades can have both positive and negative impacts on local and overall thrust production.

ACKNOWLEDGMENTS

This research was funded by the U.S. Government under Cooperative Agreement No. W911W6-21-2-0001. The U.S. Government is authorized to reproduce and distribute reprints for Government purposes notwithstanding any copyright notation thereon.

The views and conclusions contained in this document are those of the authors and should not be interpreted as

representing the official policies or position, either expressed or implied, of the U.S. Army Combat Capabilities Development Command (DEVCOM), Aviation & Missile Center (AvMC), or the U.S. Government.

Author Contacts

Wei-Han Chen: wchen669@gatech.edu
Juergen Rauleder: Juergen.Rauleder@gatech.edu

REFERENCES

1. Sydney, A., Ramsey, J., and Kimmel, K., “Experimental investigation of the turbulent aerodynamic environment produced by a generic ship,” 54th AIAA Aerospace Sciences Meeting, 2016. DOI: 10.2514/6.2016-1071.
2. Seth, D., Leishman, J. G., Gnanamanickam, E., and Zhang, Z., “Time-resolved ship airwake measurements in a simulated atmospheric boundary layer,” *Journal of Aircraft*, Vol. 58, (3), 2021, pp. 624–649. DOI: 10.2514/1.C035886.
3. Zhu, N., Zhang, Z., Gnanamanickam, E., and Gordon Leishman, J., “Space-time characterization of ship airwakes,” *AIAA Journal*, Vol. 61, (2), 2023, pp. 681–697. DOI: 10.2514/1.J062093.
4. Mazzilli, G., Zhang, Z., Gnanamanickam, E., and Leishman, J., “Comparison of NATO-GD and SFS2 Ship Airwakes Using Low-Rank Models,” APS Division of Fluid Dynamics Meeting Abstracts, 2024.
5. Owen, I., Lee, R., Wall, A., and Fernandez, N., “The NATO generic destroyer—a shared geometry for collaborative research into modelling and simulation of shipboard helicopter launch and recovery,” *Ocean Engineering*, Vol. 228, 108428, 2021. DOI: 10.1016/j.oceaneng.2020.108428.
6. Palm, K. H., Mazzilli, G. A., Zhang, Z., Gnanamanickam, E. P., and Leishman, J. G., “Characterization of Flow Structures Within the Airwake of NATO Generic Destroyer,” AIAA SciTech 2025 Forum, 2025. DOI: 10.2514/6.2025-1077.
7. Zan, S. J., “Experimental determination of rotor thrust in a ship airwake,” *Journal of the American Helicopter Society*, Vol. 47, (2), April 2002, pp. 100–108. DOI: 10.4050/JAHS.47.100.
8. Lee, R. G., and Zan, S. J., “Wind tunnel testing of a helicopter fuselage and rotor in a ship airwake,” *Journal of the American Helicopter Society*, Vol. 50, (4), October 2005, pp. 326–337. DOI: 10.4050/1.3092869.
9. Silva, M. J., Yamauchi, G. K., Wadcock, A. J., and Long, K. R., “Wind tunnel investigation of the aerodynamic interactions between helicopters and tiltrotors in a shipboard environment,” Proceedings of the American Helicopter Society 4th Decennial Specialist’s Conference on Aeromechanics, San Francisco, CA, January 21–23, 2004.
10. Wang, Y., Curran, J., Padfield, G., and Owen, I., “AirDyn: an instrumented model-scale helicopter for measuring unsteady aerodynamic loading in airwakes,”

- Measurement Science and Technology*, Vol. 22, (4), 045901, 2011. DOI: 10.1088/0957-0233/22/4/045901.
11. Kääriä, C. H., Wang, Y., White, M. D., and Owen, I., "An experimental technique for evaluating the aerodynamic impact of ship superstructures on helicopter operations," *Ocean Engineering*, Vol. 61, 2013, pp. 97–108. DOI: 10.1016/j.oceaneng.2012.12.052.
 12. Nacakli, Y., Landman, D., and Doane, S., "Investigation of backward-facing-step flow field for dynamic interface application," *Journal of the American Helicopter Society*, Vol. 57, 032005(2012), 2012. DOI: 10.4050/JAHS.57.032005.
 13. Taymourtash, N., Zagaglia, D., Zanotti, A., Muscarello, V., Gibertini, G., and Quaranta, G., "Experimental study of a helicopter model in shipboard operations," *Aerospace Science and Technology*, Vol. 115, 106774, 2021. DOI: 10.1016/j.ast.2021.106774.
 14. Silva, M., Schatzman, D., and Ramasamy, M., "Sub-Scale Investigation of Coupled Rotor/ Upwind Ship Aerodynamic Interactions," Proceedings of the 6th Decennial VFS Aeromechanics Specialists' Conference, Santa Clara, CA, February 6–8, 2024.
 15. Forrest, J., Kaaria, C., and Owen, I., "Evaluating ship superstructure aerodynamics for maritime helicopter operations through CFD and flight simulation," *The Aeronautical Journal*, Vol. 120, (1232), 2016, pp. 1578–1603. DOI: 10.1017/aer.2016.76.
 16. Ashok, S. G., and Rauleder, J., "Mid-fidelity NATO generic destroyer static and moving-ship airwake simulations using the Lattice-Boltzmann method compared with experimental data," *Ocean Engineering*, Vol. 298, 117264, 2024. DOI: 10.1016/j.oceaneng.2024.117264.
 17. Kurban, E., Oates, B., Smith, M. J., and Rauleder, J., "Correlation of High-and Mid-Fidelity Ship Airwake Analysis to Experiment," *Journal of Aircraft*, 2025, pp. 1–18. DOI: 10.2514/1.C038087.
 18. Kurban, E., Toxopeus, S., and Rauleder, J., "Assessment of Lattice-Boltzmann velocity set and floating-point precision for ship airwake analysis compared to RANS–LES and experiment," *Ocean Engineering*, Vol. 326, 2025, pp. 120788. DOI: 10.1016/j.oceaneng.2025.120788.
 19. Fernandez, N., Watson, N., Owen, I., and White, M., "A Comparative Assessment of the NATO-GD and SFS2 Ship Airwakes and their Influence upon Helicopter Aerodynamic Loading," Proceedings of the 78th Annual Forum of the Vertical Flight Society, Fort Worth, TX, May 10–12, 2022. DOI: 10.4050/F-0078-2022-17584.
 20. Ashok, S. G., and Rauleder, J., "Real-Time Coupled Ship-Rotorcraft Interactional Simulations Using GPU-Accelerated Lattice-Boltzmann Method," *Journal of the American Helicopter Society*, Vol. 70, (2), 2025, pp. 1–25. DOI: 10.4050/JAHS.70.022005.
 21. Chen, W. H., and Rauleder, J., "Unsteady Loads of a Scaled Rotor on and near the Landing Deck of the NATO Generic Destroyer with Concurrent Stereo PIV and Surface Pressure Measurements," *Journal of the American Helicopter Society*, Vol. 69, (4), 2024. DOI: 10.4050/JAHS.69.042008.
 22. Barlow, J. B., Rae, W. H., and Pope, A., *Low-speed wind tunnel testing*, John Wiley & Sons, New York, NY, 1999, p. 374.
 23. NATO AVT-315 Task Group, "Comparative Assessment of Modelling and Simulation Methods of Shipboard Launch and Recovery of Helicopters," Technical Report STO-TR-AVT-315, 2023. DOI: 10.14339/STO-TR-AVT-315.
 24. Healey, J. V., "Establishing a database for flight in the wakes of structures," *Journal of Aircraft*, Vol. 29, (4), 1992, pp. 559–564. DOI: 10.2514/3.46202.
 25. Rosenfeld, N., Kimmel, K., and Sydney, A. J., "Investigation of ship topside modeling practices for wind tunnel experiments," Proceedings of the 53rd AIAA Aerospace Sciences Meeting, Kissimmee, FL, January 5–9, 2015, 0245. DOI: 10.2514/6.2015-0245.
 26. MilliporeSigma, "S1402 Safety Data Sheet – Sulforhodamine B sodium salt," 2024, <https://www.sigmaldrich.com/US/en/sds/sigma/s1402>.
 27. MilliporeSigma, "R4127 Safety Data Sheet – Rhodamine 6G," 2025, <https://www.sigmaldrich.com/US/en/sds/sigma/r4127>.
 28. MilliporeSigma, "R6626 Safety Data Sheet – Rhodamine B," 2024, <https://www.sigmaldrich.com/US/en/sds/sigma/r6626>.
 29. Petrosky, B., Lowe, K., Danehy, P., Wohl, C., and Tiemsin, P., "Improvements in laser flare removal for particle image velocimetry using fluorescent dye-doped particles," *Measurement Science and Technology*, Vol. 26, (11), 2015, pp. 115303. DOI: 10.1088/0957-0233/26/11/115303.
 30. McRuer, D. T., "Interdisciplinary interactions and dynamic systems integration," *International Journal of Control*, Vol. 59, (1), 1994, pp. 3–12. DOI: 10.1080/00207179408923067.
 31. McTavish, S., Wall, A., and Lee, R., "A Methodology to Correlate Simulated Airwake Data and Unsteady Helicopter Load Measurements to Shipboard Helicopter Flight Test Data," Proceedings of the 14th International Conference on Wind Engineering, Porto Alegre, Brazil, June 21–26, 2015.
 32. Taylor, G. I., "The spectrum of turbulence," *Proceedings of the Royal Society of London. Series A-Mathematical and Physical Sciences*, Vol. 164, (919), 1938, pp. 476–490. DOI: 10.1098/rspa.1938.0032.
 33. Deng, S., Percin, M., and van Oudheusden, B., "Experimental investigation of aerodynamics of flapping-wing micro-air-vehicle by force and flow-field measurements," *AIAA Journal*, Vol. 54, (2), 2016, pp. 588–602. DOI: 10.2514/1.J054403.